



저작자표시-비영리-동일조건변경허락 2.0 대한민국

이용자는 아래의 조건을 따르는 경우에 한하여 자유롭게

- 이 저작물을 복제, 배포, 전송, 전시, 공연 및 방송할 수 있습니다.
- 이차적 저작물을 작성할 수 있습니다.

다음과 같은 조건을 따라야 합니다:



저작자표시. 귀하는 원저작자를 표시하여야 합니다.



비영리. 귀하는 이 저작물을 영리 목적으로 이용할 수 없습니다.



동일조건변경허락. 귀하가 이 저작물을 개작, 변형 또는 가공했을 경우에는, 이 저작물과 동일한 이용허락조건하에서만 배포할 수 있습니다.

- 귀하는, 이 저작물의 재이용이나 배포의 경우, 이 저작물에 적용된 이용허락조건을 명확하게 나타내어야 합니다.
- 저작권자로부터 별도의 허가를 받으면 이러한 조건들은 적용되지 않습니다.

저작권법에 따른 이용자의 권리는 위의 내용에 의하여 영향을 받지 않습니다.

이것은 [이용허락규약\(Legal Code\)](#)을 이해하기 쉽게 요약한 것입니다.

[Disclaimer](#)

공학석사 학위논문

**Frequency-domain acoustic and
elastic modeling and waveform
inversion in the logarithmic grid set**

로그 격자군을 이용한 주파수 영역에서의
음향파 및 탄성파 모델링과 파형 역산

2013 년 2 월

서울대학교 대학원

에너지시스템공학부

최 승 우

Frequency-domain acoustic and elastic modeling and waveform inversion in the logarithmic grid set

로그 격자군을 이용한 주파수 영역에서의
음향파 및 탄성파 모델링과 파형 역산

지도 교수 민 동 주

이 논문을 공학석사 학위논문으로 제출함
2012 년 12 월

서울대학교 대학원
에너지시스템공학부
최 승 우

최승우의 공학석사 학위논문을 인준함
2013 년 1 월

위 원 장 _____ (인)

부위원장 _____ (인)

위 원 _____ (인)

Abstract

One of the factors influence the accuracy of seismic modeling is boundary condition. Several boundary conditions have been developed and have their own advantages and disadvantages. One possible method to perfectly remove edge reflections is to extend the dimension of a given model so that edge reflections cannot be recorded within the recording duration. To make the idea feasible without increasing computational costs, we propose acoustic and elastic modeling algorithms performed in the logarithmic grid set, where grid size increases logarithmically from the middle of model surface. This method has an advantage to reduce the number of grids by the property of logarithmic scale. For acoustic and elastic wave modeling in the logarithmic grid set, the wave equations are first converted from the uniform scale to the logarithm scale. Then we apply the conventional node-based finite-difference method for the acoustic case and the cell-based finite-difference method for elastic case. Numerical examples show that the new modeling algorithms yield solutions comparable to those of the conventional modeling algorithm, although they can suffer from numerical dispersion when the source is located in the coarse grids (far from the origin). Inversion results for the simple layered model and the modified version of the Marmousi-2 model show that the logarithmic inversion algorithms yield results comparable to those obtained by the conventional inversion achieving computational efficiency when the recording duration is not too long and the influence of numerical dispersion is almost negligible in the inversion.

Keywords: acoustic, elastic, seismic modeling, waveform inversion,
logarithmic grid set

Student number: 2011-21113

Contents

Abstract	i
Contents.....	iii
List of figures	iv
List of tables	vii
1. Introduction	1
2. Modeling.....	4
2.1. Acoustic wave equation on the logarithmic scale.....	4
2.2. Finite-difference method.....	7
2.3. Elastic wave equation on the logarithmic scale.....	8
2.4. Cell-based finite-difference method.....	10
2.5. Example of modeling in the logarithmic grid set	14
3. Waveform inversion	21
3.1. Gradient method.....	21
3.2. Verification of virtual source.....	22
3.3. Scaling and optimization.....	31
3.4. Example of inversion in the logarithmic grid set	32
4. Conclusions	43
References.....	45
Abstract (In Korean)	48

List of figures

Figure 1. the logarithmic functions shifted in order to pass the origin for (a) positive x and (b) negative x	5
Figure 2. Grid sets used to obtain the finite-difference solutions for the (i, j) th nodal point inside the main body. Lamé constants (represented as k) and first-order partial derivative of displacement are defined within the cells ...	11
Figure 3. The geometry of the semi-infinite homogeneous model for Lamb's problem.....	12
Figure 4. Horizontal (left) and vertical displacements (right) of analytic (solid line) and numerical solutions obtained in the logarithmic grid set (dashed line) at distances of 50, 200 and 400 m from the source point.....	13
Figure 5. P-wave velocity models for the modified version of Marmousi-2 model on the (a) conventional uniform and (b) logarithmic scales.....	15
Figure 6. Synthetic seismograms of pressure obtained in the conventional grid set (a), converted through interpolation from the conventional to the logarithmic grid set (b) and obtained in the logarithmic grid set (c).....	16
Figure 7. Comparison of traces extracted at distances of 3.15 km and 5.85 km of the seismograms for pressure (Figure 6) obtained in the conventional (solid line) and logarithmic (dashed line) grid sets	17
Figure 8. Synthetic seismograms of horizontal displacements obtained in the conventional grid set, converted through interpolation from the conventional to the logarithmic grid set and obtained in the logarithmic grid set	18
Figure 9. Synthetic seismograms of vertical displacements obtained in the	

conventional grid set, converted through interpolation from the conventional to the logarithmic grid set and obtained in the logarithmic grid set	19
Figure 10. Comparison of traces extracted at distances of 3.15 km, 4.5 km and 5.85 km of the seismograms for horizontal (upper) and vertical (lower) displacements (Figure 8 and 9) obtained in the conventional (solid line) and logarithmic (dashed line) grid sets	20
Figure 11. arrangement of the source and perturbation grid for verification of virtual source in the (a) left- and (b) right-side of the homogeneous and isotropic model	23
Figure 12. seismograms of partial derivative wavefields for c obtained by numerical and analytic methods for the left-side of the model	24
Figure 13. seismograms of partial derivative wavefields for c obtained by numerical and analytic methods for the right-side of the model	24
Figure 14. seismograms of partial derivative wavefields for λ obtained by numerical and analytic methods for the right-side of the model: horizontal(upper) and vertical(lower) displacements	25
Figure 15. seismograms of partial derivative wavefields for λ obtained by numerical and analytic methods for the left-side of the model: horizontal(upper) and vertical(lower) displacements	26
Figure 16. seismograms of partial derivative wavefields for μ obtained by numerical and analytic methods for the left-side of the model: horizontal(upper) and vertical(lower) displacements	27
Figure 17. seismograms of partial derivative wavefields for μ obtained by	

numerical and analytic methods for the right-side of the model: horizontal(upper) and vertical(lower) displacements	28
Figure 18. partial derivative wavefields of c recorded at the middle of the model for the left- and right-side of the model.....	29
Figure 19. partial derivative wavefields of λ recorded at the middle of the model for the left- and right-side of the model: horizontal(upper) and vertical(lower) displacements.....	29
Figure 20. partial derivative wavefields of μ recorded at the middle of the model for the left- and right-side of the model: horizontal(upper) and vertical(lower) displacements.....	30
Figure 21. (a) True simple layered velocity model and inversion results obtained at the 200th iteration by using the (b) conventional and (c) logarithmic grid sets. For comparison, the logarithmic inversion result (c) is converted to the conventional grid set in (d)	35
Figure 22. Depth profiles at the center of the true velocity model (solid line) and the inverted velocity models generated in the conventional (dotted line) and logarithmic (dashed line) grid sets	36
Figure 23. Inversion results obtained at the 200th iteration by using the (a) conventional and (b) logarithmic grid sets. For comparison, the logarithmic inversion result (b) is converted to the conventional grid set in (c)	38
Figure 24. Depth profiles at distances of (a) 4.5 km and (b) 6 km of the true velocity model (solid line) and the inverted velocity models generated in the conventional (dotted line) and logarithmic (dashed line) grid sets.....	39

Figure 25. (a) P-wave velocity models inverted at the 200th iteration in the logarithmic grid set for the modified version of the Marmousi-2 model and (b) its interpolated version to the conventional grid set.....	41
Figure 26. Depth profiles at distances of (a) 4.5 km and (b) 6 km of the true velocity model (solid line) and the inverted velocity models.....	42

List of tables

Table 1. CPU times required to perform the acoustic inversion for the simple layered model and the Marmousi-2 model for 200th iteration.....	41
---	----

1. Introduction

Seismic modeling, which is a good tool to describe seismic wave propagation in subsurface media, is also used in seismic inversion and migration. Since seismic modeling is iteratively conducted in seismic inversion and migration, the accuracy and efficiency of seismic inversion and migration depend largely on those of seismic modeling.

These days, seismic modeling has mainly been performed using the discrete methods such as finite-difference and finite-element methods, where boundary conditions are necessary to suppress the edge reflections arising from finite-sized models unlike real media. Several boundary conditions have been developed. Reynolds (1977), Clayton and Engquist (1978) and Higdon (1991) proposed applying one-way wave equations so that incoming waves are not generated and only outgoing waves can propagate through boundaries. In this case, however, since one-way wave equations render the modeling operator asymmetrical, modeling algorithms do not satisfy the reciprocity theorem unlike in the real earth. Cerjan (1985) defined damping areas surrounding a given model, where amplitudes of waves gradually decrease. The perfectly matched layer method (Collino and Tsogka, 2001) eliminates edge reflections in the similar way. These damping methods increase computational costs due to the additional damping areas. However, even though we apply the aforementioned boundary conditions, edge reflections are not perfectly removed. To perfectly remove edge reflections, we may want to extend the given model so that edge reflections cannot return to receivers within the recording duration. In that case, however, we need a lot of

computational efforts. To alleviate computational overburden, the variable grid sets are necessary.

In seismic modeling using the finite-difference or finite-element methods, grid sizes are determined by the maximum frequency and the minimum velocity of given models to minimize numerical dispersions of waves for the entire model. In general, as waves propagate through subsurface media, high-frequency components easily attenuate because of intrinsic absorption. In addition, velocities are usually higher in the deeper part than in the shallow part. As a result, grid sizes suitable for low velocity regions near source points may be redundant for regions far from source positions. Based on this feature, non-uniform grid sets have been proposed to reduce computational costs. Moczo (1989) introduced irregular grids whose size is horizontally constant but vertically varying for SH-waves in 2D heterogeneous media. Jastram and Tessmer (1994) used discontinuous grids where the horizontal spacing changes abruptly and vertical spacing becomes gradually coarser on a staggered grid set.

In this study, we propose a new grid set called ‘logarithmic grid set’, where grid spacing increases logarithmically with distance from the middle of the surface of a given model and apply it in modeling and inversion algorithms. Using the logarithmic grid set, we can make edge reflections not recorded within the total recording time, which allows us to efficiently obtain edge-reflection-free modeling results without any boundary conditions. In the following sections, we first introduce how the acoustic and elastic wave equations and the source positions in the uniform grid set can be transformed

into the logarithmic grid. Next, we verify the modeling operators composed in the logarithmic grid set by comparing them with those composed in the conventional grid set and then apply it to the acoustic and elastic waveform inversion. For waveform inversion, we apply the gradient method based on the adjoint state of modeling operator (e.g., Lailly, 1983; Tarantola, 1984; Pratt et al., 1998) and use the pseudo-Hessian matrix to scale the gradient (Shin et al., 2001). The modeling and inversion algorithms are applied to a simple layered model and the modified version of the Marmousi-2 model (Martin et al., 2006).

2. Modeling

2.1. Acoustic wave equation on the logarithmic scale

In the time domain, the 2D acoustic wave equation can be written as

$$\frac{1}{c^2} \frac{\partial^2 p}{\partial t^2} = \frac{\partial^2 p}{\partial x^2} + \frac{\partial^2 p}{\partial z^2} + \delta(x - x_0) \delta(z - z_0) f \quad (1)$$

where $c(x, z)$ is subsurface velocity, $p(x, z, t)$ is pressure field, $f(t)$ is source wavelet function. $\delta(x - x_0)$ and $\delta(z - z_0)$ are delta functions locating a source in (x_0, z_0) . Fourier-transforming eq. (1) gives the 2D acoustic wave equation in the frequency domain, as follows

$$-\frac{\omega^2}{c^2} \tilde{p} = \frac{\partial^2 \tilde{p}}{\partial x^2} + \frac{\partial^2 \tilde{p}}{\partial z^2} + \delta(x - x_0) \delta(z - z_0) \tilde{f} \quad , \quad (2)$$

where

$$\tilde{p}(x, z, \omega) = \frac{1}{\sqrt{2\pi}} \int_{-\infty}^{\infty} p(x, z, t) e^{-i\omega t} dt \quad , \quad (3)$$

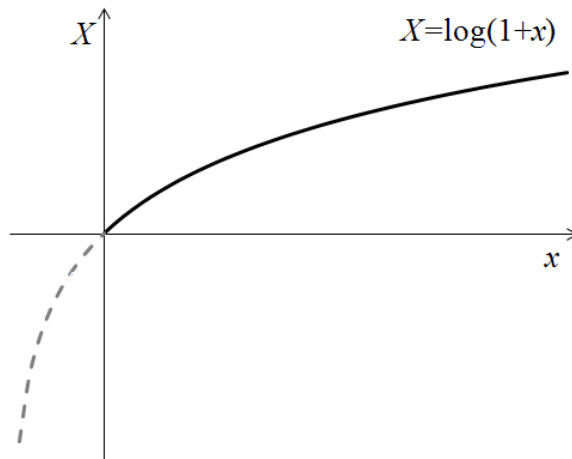
$$\tilde{f}(\omega) = \frac{1}{\sqrt{2\pi}} \int_{-\infty}^{\infty} f(t) e^{-i\omega t} dt \quad , \quad (4)$$

and ω is angular frequency,

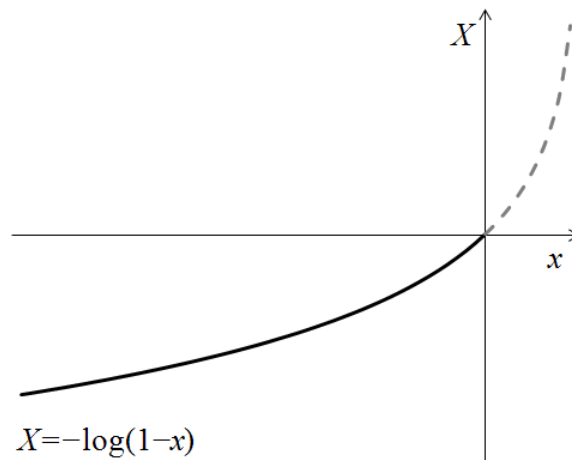
The acoustic wave equation (eq. 2) is converted to the logarithmic grid set by using the logarithmic functions shifted in order to pass the origin (Fig. 1) and making parameters. The origin corresponds to the middle of the model surface.

$$X = g(x) = \begin{cases} \log(1+x), & x \geq 0 \\ -\log(1-x), & x < 0 \end{cases} \quad , \quad (5)$$

$$Z = h(z) = \log(1+z) \quad . \quad (6)$$



(a)



(b)

Figure 1. the logarithmic functions shifted in order to pass the origin for (a) positive x and (b) negative x

These parameters change terms containing differential operators as

$$\frac{\partial \tilde{p}}{\partial x} = \begin{cases} \frac{1}{e^x} \frac{\partial \tilde{p}}{\partial X}, & x \geq 0 \\ e^x \frac{\partial \tilde{p}}{\partial X}, & x < 0 \end{cases}, \quad (7)$$

$$\frac{\partial \tilde{p}}{\partial Z} = \frac{1}{e^Z} \frac{\partial \tilde{p}}{\partial Z}, \quad (8)$$

$$\frac{\partial^2 \tilde{p}}{\partial x^2} = \begin{cases} \frac{1}{e^{2x}} \frac{\partial^2 \tilde{p}}{\partial X^2} - \frac{1}{e^{2x}} \frac{\partial \tilde{p}}{\partial X}, & x \geq 0 \\ e^{2x} \frac{\partial^2 \tilde{p}}{\partial X^2} + e^{2x} \frac{\partial \tilde{p}}{\partial X}, & x < 0 \end{cases}, \quad (9)$$

$$\frac{\partial^2 \tilde{p}}{\partial z^2} = \frac{1}{e^{2Z}} \frac{\partial^2 \tilde{p}}{\partial Z^2} - \frac{1}{e^{2Z}} \frac{\partial \tilde{p}}{\partial Z}. \quad (10)$$

The source can be located in the logarithmic grids by the intrinsic property of delta function as,

$$\delta(g^{-1}(X)) = \frac{\delta(X - X_0)}{|g^{-1}'(X_0)|} = \begin{cases} \frac{\delta(X - X_0)}{e^{X_0}}, & x \geq 0 \\ \frac{\delta(X - X_0)}{e^{-X_0}}, & x < 0 \end{cases}, \quad (11)$$

$$\delta(h^{-1}(Z)) = \frac{\delta(Z - Z_0)}{|h^{-1}'(Z_0)|} = \frac{\delta(Z - Z_0)}{e^{Z_0}}. \quad (12)$$

Applying equations (9) ~ (12) to equations (2) gives the 2D acoustic wave equation for positive x in the logarithm-scaled coordinate, as follows

$$-\frac{\omega^2}{c^2} \tilde{p} = \frac{1}{e^{2x}} \left(\frac{\partial^2 \tilde{p}}{\partial X^2} - \frac{\partial \tilde{p}}{\partial X} \right) + \frac{1}{e^{2Z}} \left(\frac{\partial^2 \tilde{p}}{\partial Z^2} - \frac{\partial \tilde{p}}{\partial Z} \right) + \frac{\delta(X - X_0)}{e^{X_0}} \frac{\delta(Z - Z_0)}{e^{Z_0}} \tilde{f}. \quad (13)$$

In the same way, the wave equation for negative x in the logarithm-scaled coordinate can be obtained as follows

$$-\frac{\omega^2}{c^2} \tilde{p} = e^{2X} \left(\frac{\partial^2 \tilde{p}}{\partial X^2} + \frac{\partial \tilde{p}}{\partial X} \right) + \frac{1}{e^{2Z}} \left(\frac{\partial^2 \tilde{p}}{\partial Z^2} - \frac{\partial \tilde{p}}{\partial Z} \right) + \frac{\delta(X - X_0)}{e^{-X_0}} \frac{\delta(Z - Z_0)}{e^{Z_0}} \tilde{f}. \quad (14)$$

2.2. Finite-difference method

For acoustic modeling, we discretize the modified acoustic wave equations, i.e., equations (13) and (14) by numerical methods, such as finite-difference and finite-element method. Among them, since finite-difference approach is simply and readily implemented, Kelly et al. (1976) adopted it to make synthetic seismograms in the time domain. In the frequency domain, finite-difference method allows us to effectively obtain solutions to the wave equation for additional source positions (Pratt, 1990). By second-order finite-difference method, the finite-difference acoustic wave equation in the logarithmic grid set for positive x is

$$\begin{aligned} & -\frac{\omega^2}{c_{i,j}^2} \tilde{p}_{i,j} - \frac{1}{e^{2i\Delta X}} \left(\frac{\tilde{p}_{i+1,j} - \tilde{p}_{i,j} + \tilde{p}_{i-1,j}}{(\Delta X)^2} - \frac{\tilde{p}_{i+1,j} - \tilde{p}_{i-1,j}}{2\Delta X} \right) \\ & - \frac{1}{e^{2j\Delta Z}} \left(\frac{\tilde{p}_{i,j+1} - \tilde{p}_{i,j} + \tilde{p}_{i,j-1}}{(\Delta Z)^2} - \frac{\tilde{p}_{i,j+1} - \tilde{p}_{i,j-1}}{2\Delta Z} \right) \\ & = \frac{\delta(X - X_0)}{e^{j_0\Delta X}} \frac{\delta(Z - Z_0)}{e^{j_0\Delta Z}} \tilde{f} \end{aligned} \quad , \quad (15)$$

where i and j are grid number of X and Z direction and $\Delta X, \Delta Z$ is grid size. In

this case, the range of grid number of s direction is $0 \leq i \leq \frac{nX}{2}$, when the

number of grid in x direction is $nX + 1$. In the same way, for negative x in the logarithm-scaled coordinate, the acoustic wave equation can be discretized by

$$\begin{aligned}
& -\frac{\omega^2}{c_{i,j}^2} \tilde{p}_{i,j} - e^{2i\Delta X} \left(\frac{\tilde{p}_{i+1,j} - \tilde{p}_{i,j} + \tilde{p}_{i-1,j}}{(\Delta X)^2} + \frac{\tilde{p}_{i+1,j} - \tilde{p}_{i-1,j}}{2\Delta X} \right) \\
& - \frac{1}{e^{2j\Delta Z}} \left(\frac{\tilde{p}_{i,j+1} - \tilde{p}_{i,j} + \tilde{p}_{i,j-1}}{(\Delta Z)^2} - \frac{\tilde{p}_{i,j+1} - \tilde{p}_{i,j-1}}{2\Delta Z} \right) \quad (16) \\
& = \frac{\delta(X - X_0)}{e^{-i_0\Delta X}} \frac{\delta(Z - Z_0)}{e^{j_0\Delta Z}} \tilde{f}
\end{aligned}$$

In this case, the range of grid number of s direction is $-\frac{nX}{2} \leq i < 0$, when the number of grid in x direction is $nX + 1$. Equations (15) and (16) can be written in a matrix form as

$$\mathbf{S}\mathbf{u} = \mathbf{f}, \quad (17)$$

where \mathbf{S} is the complex impedance matrix, and \mathbf{f} is the source vectors, respectively.

2.3. Elastic wave equation on the logarithmic scale

In the frequency domain, the 2D elastic wave equation can be written as

$$\begin{aligned}
-\omega^2 \rho u &= \frac{\partial}{\partial x} \left[(\lambda + 2\mu) \frac{\partial u}{\partial x} + \lambda \frac{\partial v}{\partial z} \right] + \frac{\partial}{\partial z} \left[\mu \left(\frac{\partial v}{\partial x} + \frac{\partial u}{\partial z} \right) \right] \quad (18) \\
&+ \delta(x - x_0) \delta(z - z_0) f_x
\end{aligned}$$

$$\begin{aligned}
-\omega^2 \rho v &= \frac{\partial}{\partial z} \left[(\lambda + 2\mu) \frac{\partial v}{\partial z} + \lambda \frac{\partial u}{\partial x} \right] + \frac{\partial}{\partial x} \left[\mu \left(\frac{\partial u}{\partial z} + \frac{\partial v}{\partial x} \right) \right] \quad (19) \\
&+ \delta(x - x_0) \delta(z - z_0) f_z
\end{aligned}$$

where $u(x, z, \omega)$ and $v(x, z, \omega)$ are the Fourier-transformed horizontal and vertical displacements, respectively, $\rho(x, z)$ is the density, $\lambda(x, z)$ and $\mu(x, z)$ are the Lamé constants for isotropic media, and f_x and f_z are the horizontal and vertical forces, respectively.

According to equations (5) and (6), the differential operators in equations (18) and (19) can be expressed on the logarithmic scale as

$$\frac{\partial}{\partial x} \left(k \frac{\partial u}{\partial x} \right) = \begin{cases} \frac{1}{e^{2X}} \frac{\partial u}{\partial X} \left(k \frac{\partial u}{\partial X} \right) - \frac{1}{e^{2X}} \left(k \frac{\partial u}{\partial X} \right), & x \geq 0 \\ e^{2X} \frac{\partial u}{\partial X} \left(k \frac{\partial u}{\partial X} \right) + e^{2X} \left(k \frac{\partial u}{\partial X} \right), & x < 0 \end{cases}, \quad (20)$$

$$\frac{\partial}{\partial z} \left(k \frac{\partial u}{\partial z} \right) = \frac{1}{e^{2Z}} \frac{\partial u}{\partial Z} \left(k \frac{\partial u}{\partial Z} \right) - \frac{1}{e^{2Z}} \left(k \frac{\partial u}{\partial Z} \right), \quad (21)$$

$$\frac{\partial}{\partial x} \left(k \frac{\partial u}{\partial z} \right) = \begin{cases} \frac{1}{e^{X+Z}} \frac{\partial u}{\partial X} \left(k \frac{\partial u}{\partial Z} \right), & x \geq 0 \\ \frac{e^X}{e^Z} \frac{\partial u}{\partial X} \left(k \frac{\partial u}{\partial Z} \right), & x < 0 \end{cases}, \quad (22)$$

$$\frac{\partial}{\partial z} \left(k \frac{\partial u}{\partial x} \right) = \begin{cases} \frac{1}{e^{X+Z}} \frac{\partial u}{\partial Z} \left(k \frac{\partial u}{\partial X} \right), & x \geq 0 \\ \frac{e^X}{e^Z} \frac{\partial u}{\partial Z} \left(k \frac{\partial u}{\partial X} \right), & x < 0 \end{cases}, \quad (23)$$

where k means Lamé constants λ , μ or $\lambda + 2\mu$.

Substituting equations (11), (12) and (20) ~ (23) into equations (18) and (19) gives the 2D elastic wave equations for the positive x axis in the logarithm-scaled coordinate, as follows

$$\begin{aligned} -\omega^2 \rho u = & \frac{1}{e^{2X}} \left[\frac{\partial}{\partial X} \left\{ (\lambda + 2\mu) \frac{\partial u}{\partial X} \right\} - (\lambda + 2\mu) \frac{\partial u}{\partial X} \right] \\ & + \frac{1}{e^{X+Z}} \left\{ \frac{\partial}{\partial X} \left(\lambda \frac{\partial v}{\partial Z} \right) + \frac{\partial}{\partial Z} \left(\mu \frac{\partial v}{\partial X} \right) \right\} \\ & + \frac{1}{e^{2Z}} \left\{ \frac{\partial}{\partial Z} \left(\mu \frac{\partial u}{\partial Z} \right) - \mu \frac{\partial u}{\partial Z} \right\} + \frac{\delta(X - X_0)}{e^{X_0}} \frac{\delta(Z - Z_0)}{e^{Z_0}} f_x \end{aligned}, \quad (24)$$

$$\begin{aligned}
-\omega^2 \rho v = & \frac{1}{e^{2Z}} \left[\frac{\partial}{\partial Z} \left\{ (\lambda + 2\mu) \frac{\partial v}{\partial Z} \right\} - (\lambda + 2\mu) \frac{\partial v}{\partial Z} \right] \\
& + \frac{1}{e^{X+Z}} \left\{ \frac{\partial}{\partial Z} \left(\lambda \frac{\partial u}{\partial X} \right) + \frac{\partial}{\partial X} \left(\mu \frac{\partial u}{\partial Z} \right) \right\} \\
& + \frac{1}{e^{2X}} \left\{ \frac{\partial}{\partial X} \left(\mu \frac{\partial v}{\partial X} \right) - \mu \frac{\partial v}{\partial X} \right\} + \frac{\delta(X - X_0)}{e^{X_0}} \frac{\delta(Z - Z_0)}{e^{Z_0}} f_z
\end{aligned} \quad (25)$$

In the same way, the wave equations for negative x in the logarithm-scaled coordinate can be obtained as follows

$$\begin{aligned}
-\omega^2 \rho u = & e^{2X} \left[\frac{\partial}{\partial X} \left\{ (\lambda + 2\mu) \frac{\partial u}{\partial X} \right\} + (\lambda + 2\mu) \frac{\partial u}{\partial X} \right] \\
& + \frac{e^X}{e^Z} \left\{ \frac{\partial}{\partial X} \left(\lambda \frac{\partial v}{\partial Z} \right) + \frac{\partial}{\partial Z} \left(\mu \frac{\partial v}{\partial X} \right) \right\} \\
& + \frac{1}{e^{2Z}} \left\{ \frac{\partial}{\partial Z} \left(\mu \frac{\partial u}{\partial Z} \right) - \mu \frac{\partial u}{\partial Z} \right\} + \frac{\delta(X - X_0)}{e^{-X_0}} \frac{\delta(Z - Z_0)}{e^{Z_0}} f_x
\end{aligned} \quad (26)$$

$$\begin{aligned}
-\omega^2 \rho v = & \frac{1}{e^{2Z}} \left[\frac{\partial}{\partial Z} \left\{ (\lambda + 2\mu) \frac{\partial v}{\partial Z} \right\} - (\lambda + 2\mu) \frac{\partial v}{\partial Z} \right] \\
& + \frac{e^X}{e^Z} \left\{ \frac{\partial}{\partial Z} \left(\lambda \frac{\partial u}{\partial X} \right) + \frac{\partial}{\partial X} \left(\mu \frac{\partial u}{\partial Z} \right) \right\} \\
& + e^{2X} \left\{ \frac{\partial}{\partial X} \left(\mu \frac{\partial v}{\partial X} \right) + \mu \frac{\partial v}{\partial X} \right\} + \frac{\delta(X - X_0)}{e^{-X_0}} \frac{\delta(Z - Z_0)}{e^{Z_0}} f_z
\end{aligned} \quad (27)$$

2.4. Cell-based finite-difference method

For elastic modeling, we also use the finite-difference method that only uses displacements rather than the staggered grid methods. In order to properly describe the stress-free boundary conditions at the free surface, we employ the cell-based finite-difference method (Min et al., 2004), where material properties are defined within the area rather than at the nodes. In Min et al.'s methods, finite differences of the first-order partial derivative of

displacement such as $k \partial u / \partial X$ are not introduced, since conventional elastic wave equations don't contain them. So, I suggest new finite differences for finite differences of the first-order partial derivative of displacement by averaging them of each cell adjacent to one grid, as follows

$$k \frac{\partial u}{\partial X} \approx \frac{1}{4} \left[k_1 \left(\frac{\partial u}{\partial X} \right)_1 + k_2 \left(\frac{\partial u}{\partial X} \right)_2 + k_3 \left(\frac{\partial u}{\partial X} \right)_3 + k_4 \left(\frac{\partial u}{\partial X} \right)_4 \right], \quad (28)$$

$$k \frac{\partial u}{\partial Z} \approx \frac{1}{4} \left[k_1 \left(\frac{\partial u}{\partial Z} \right)_1 + k_2 \left(\frac{\partial u}{\partial Z} \right)_2 + k_3 \left(\frac{\partial u}{\partial Z} \right)_3 + k_4 \left(\frac{\partial u}{\partial Z} \right)_4 \right], \quad (29)$$

where a subscript figure means location of cells adjacent to any grid (Fig. 2).

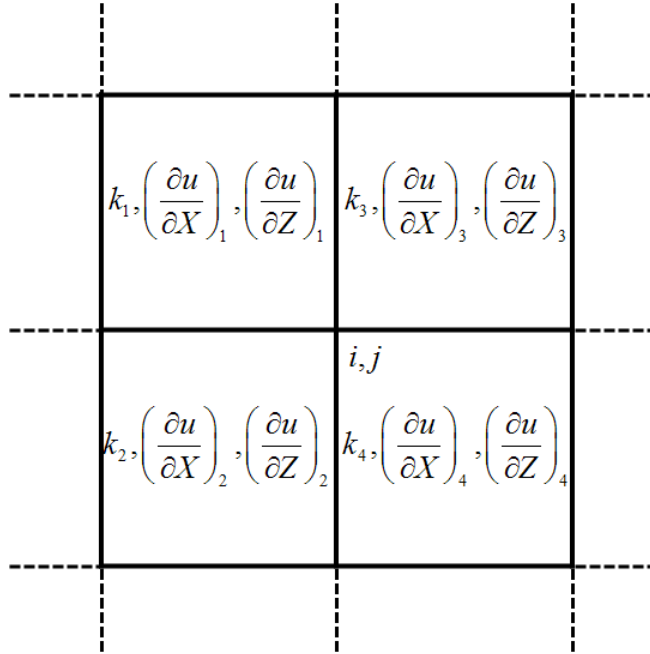


Figure 2. Grid sets used to obtain the finite-difference solutions for the (i, j) th nodal point inside the main body. Lamé constants (represented as k) and first-order partial derivative of displacement are defined within the cells.

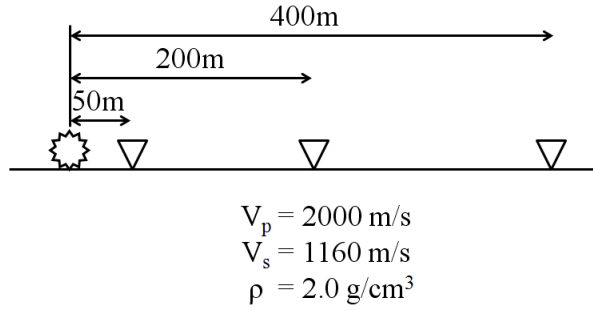


Figure 3. The geometry of the semi-infinite homogeneous model for Lamb's problem.

In order to investigate the accuracy of the elastic modeling algorithm on the logarithmic grid set, we need to compare numerical solutions with analytic solutions for Lamb's problem, for which we assume the semi-infinite homogeneous model shown in Figure 3. We compute analytic solutions referring to Ewing et al. (1957). We first compute analytic solutions in the frequency-wavenumber domain, and then take their inverse Fourier transform to obtain the time-space domain solutions. Solutions in the logarithmic grid set are obtained through interpolation. Figure 4 shows analytic solutions and numerical solutions obtained in the logarithmic grid set. From Figure 4, we see that numerical solutions agree well with analytic solutions.

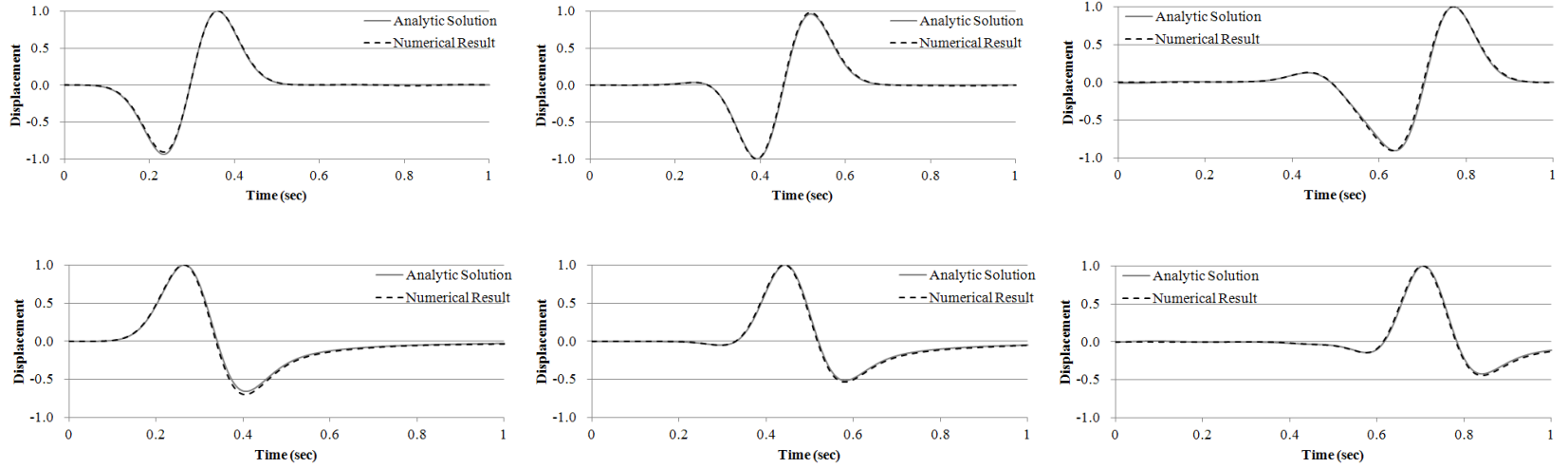


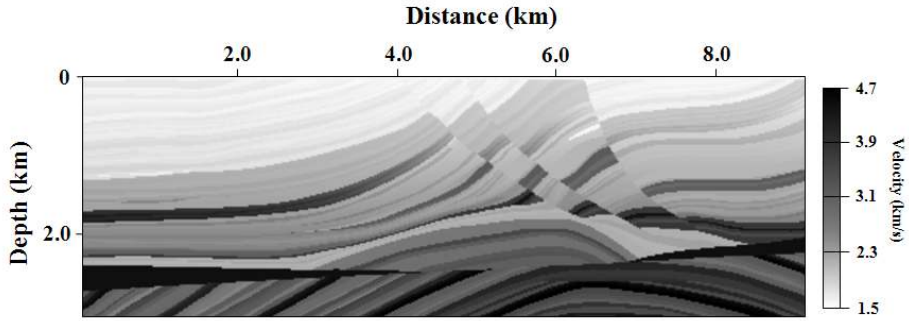
Figure 4. Horizontal (left) and vertical displacements (right) of analytic (solid line) and numerical solutions obtained in the logarithmic grid set (dashed line) at distances of 50, 200 and 400 m from the source point.

2.5. Example of modeling in the logarithmic grid set

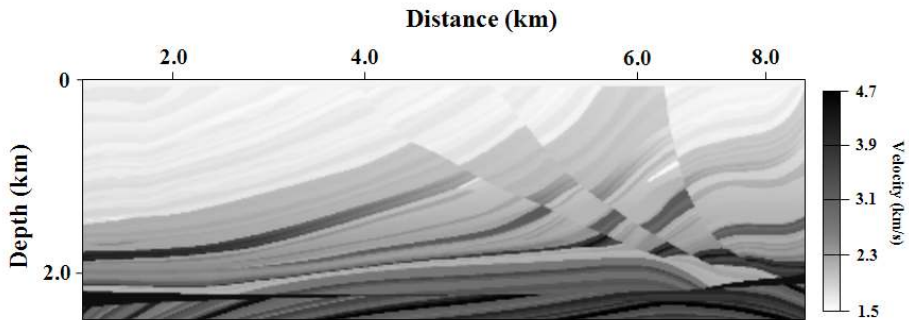
The modeling algorithms composed on the logarithmic scale are demonstrated for the modified version of the Marmousi-2 model. The model on the uniform scale is shown in Figure 2a, and Figure 2b shows the model on the logarithmic scale. The modified version of the Marmousi-2 model is obtained removing the water layer and the parts of the left- and right-hand sides. The dimension of the modified version is 9 km in width and 3.02 km in depth. Poisson's ratio and density are fixed at 0.25 and 2 g/cm^3 , respectively.

We first verify the modeling results obtained in the logarithmic grid set by comparing them with those obtained in the conventional grid set. In the logarithmic grid set, because of the nature of the logarithmic scale, the same-sized model can be simulated with fewer grid points than in the conventional grid set. Therefore, it is easy to extend the given model so that edge reflections cannot be recorded at receivers within the recording duration. For the conventional grid set, the PML boundary condition is applied to remove edge reflections, whereas in the logarithmic grid set, we do not use any boundary conditions but extend the model for boundary areas. In both the conventional and logarithmic grid sets, we use 50 additional grids for boundary areas. Grid size is 10 m for acoustic wave modeling and 5 m for elastic wave modeling. When grid space is 10 m, the total number of grids is 1001 in width and 353 in depth in the conventional grid set, whereas the number of grids is 441 in width and 190 in depth in the logarithmic grid set. In elastic case, the total number of grids is 1901 by 657 in the conventional grid set, whereas the number of grids is 783 by 330 in the logarithmic grid set.

For source wavelet, the first derivative of the Gauss function whose maximum frequency is 10 Hz is used and the maximum recording time is 4 s. Figure 2 shows seismogram of pressure in the conventional and logarithmic grid sets. In Figure 3, we compare single traces obtained in both grid sets with each other. In Figures 4 and 5, we display elastic modeling results. These results demonstrate that the modeling results obtained in the logarithmic grid set are compatible with those obtained in the conventional grid set and the interpolation is properly applied.



(a)



(b)

Figure 5. P-wave velocity models for the modified version of Marmousi-2 model on the (a) conventional uniform and (b) logarithmic scales.

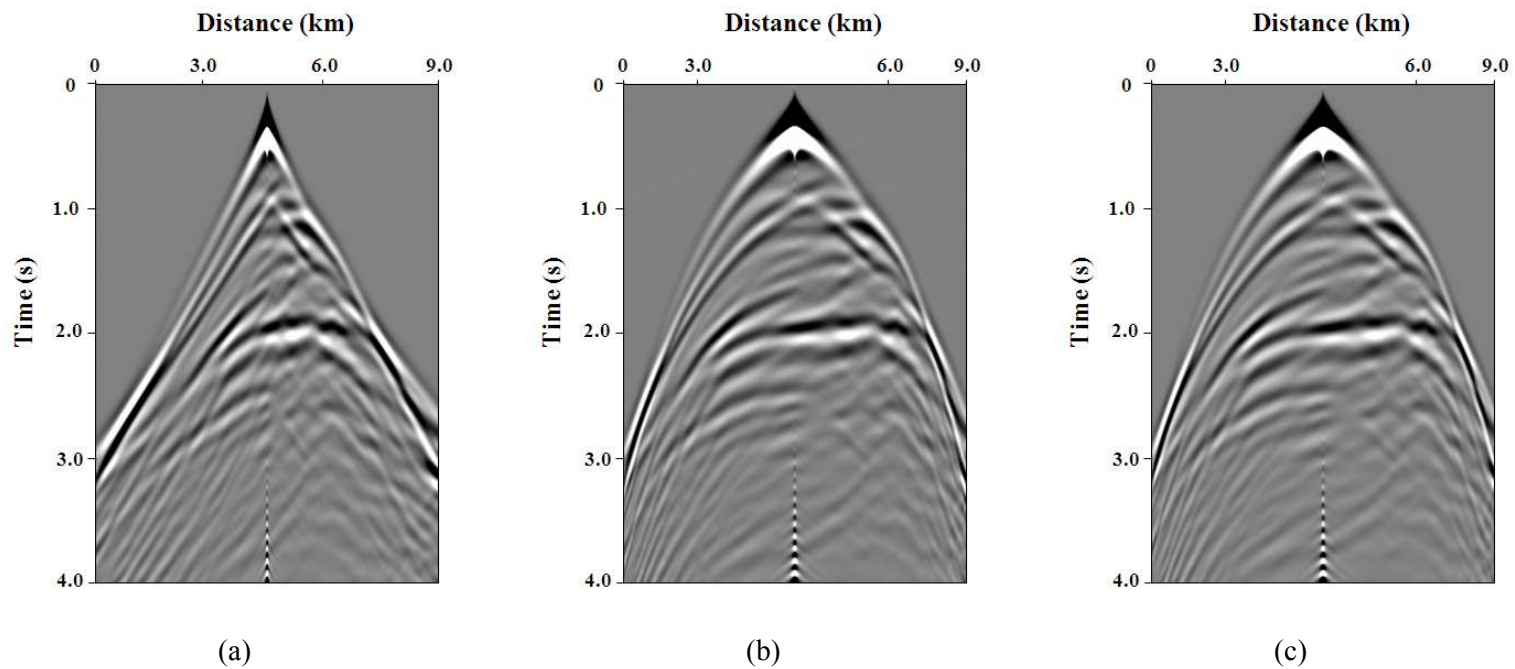


Figure 6. Synthetic seismograms of pressure obtained in the conventional grid set (a), converted through interpolation from the conventional to the logarithmic grid set (b) and obtained in the logarithmic grid set (c).

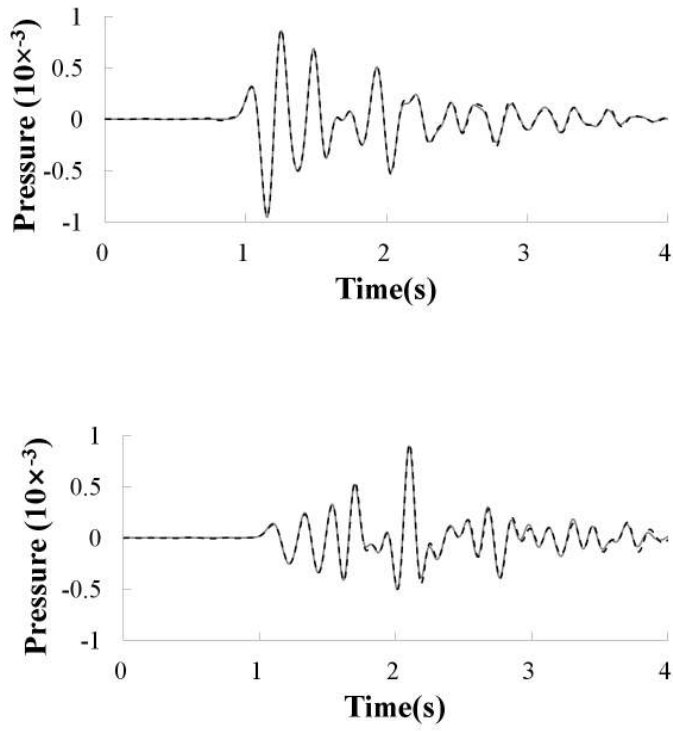


Figure 7. Comparison of traces extracted at distances of 3.15 km and 5.85 km of the seismograms for pressure (Figure 6) obtained in the conventional (solid line) and logarithmic (dashed line) grid sets.

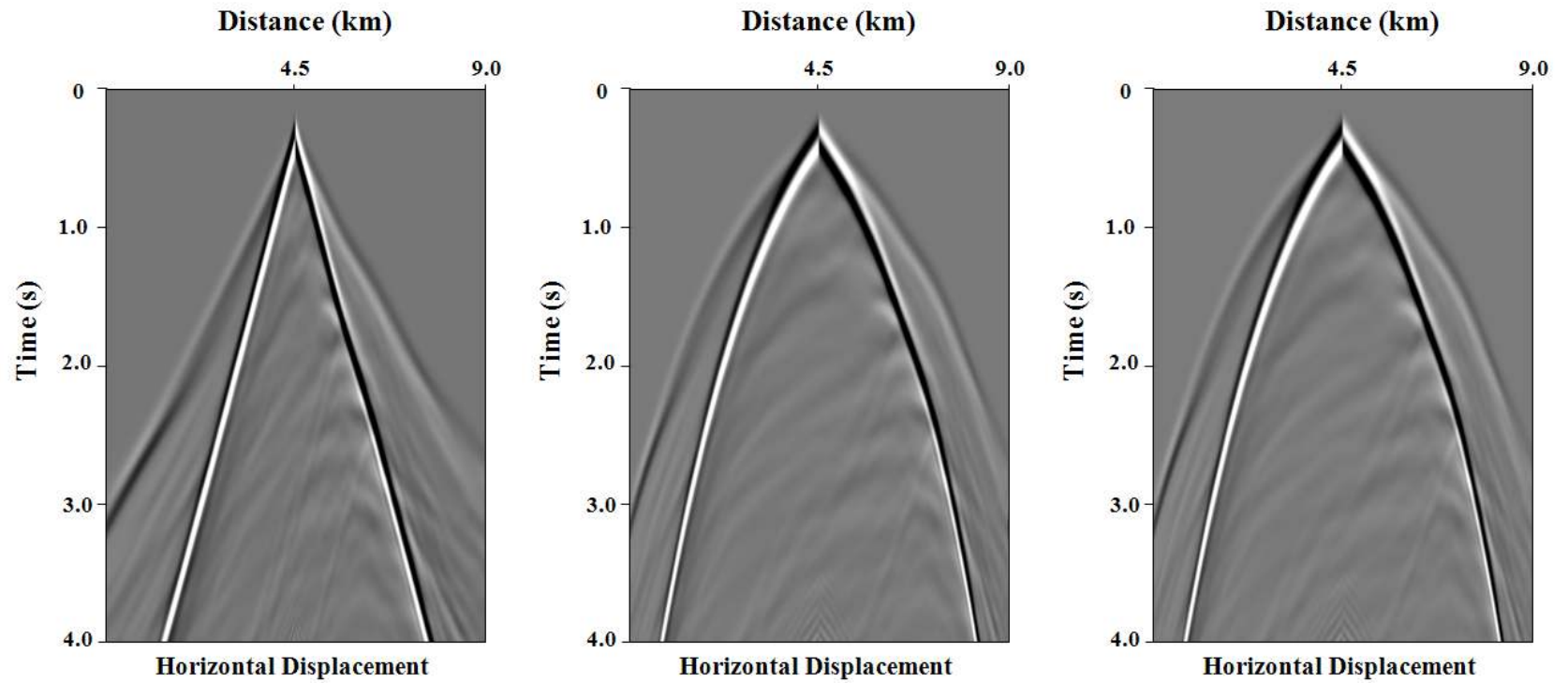


Figure 8. Synthetic seismograms of horizontal displacements obtained in the conventional grid set, converted through interpolation from the conventional to the logarithmic grid set and obtained in the logarithmic grid set.

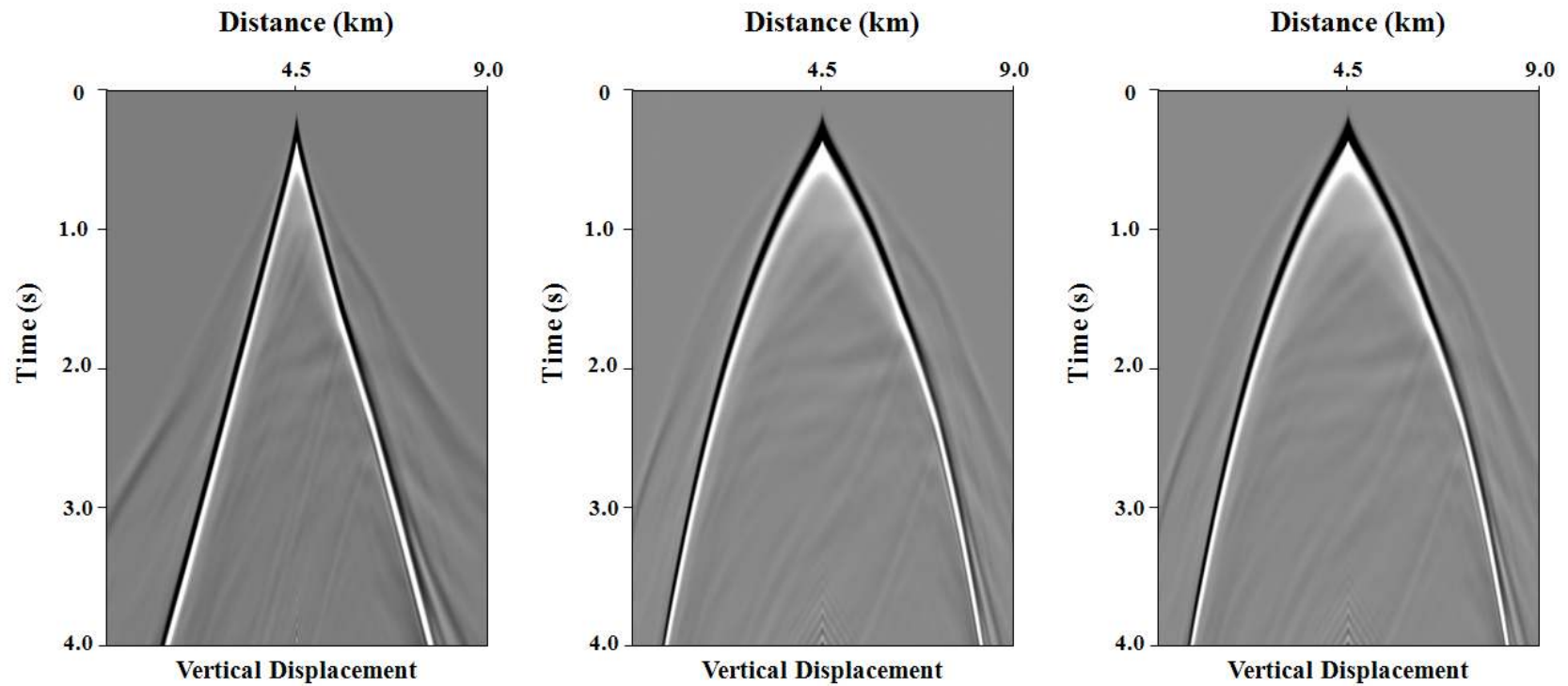


Figure 9. Synthetic seismograms of vertical displacements obtained in the conventional grid set, converted through interpolation from the conventional to the logarithmic grid set and obtained in the logarithmic grid set.

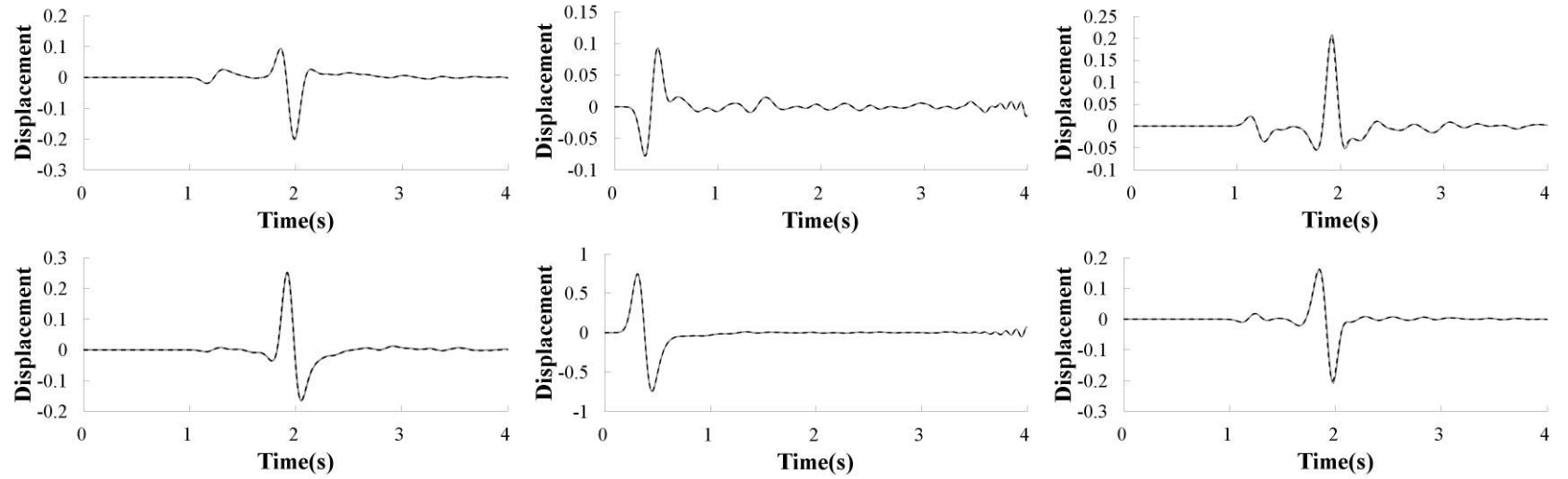


Figure 10. Comparison of traces extracted at distances of 3.15 km, 4.5 km and 5.85 km of the seismograms for horizontal (upper) and vertical (lower) displacements (Figure 8 and 9) obtained in the conventional (solid line) and logarithmic (dashed line) grid sets.

3. Waveform inversion

3.1. Gradient method

For acoustic and elastic waveform inversion, we build the objective function based on the l_2 -norm of residuals between model responses and observed data and minimize the objective function using the gradient method. For simplicity, if we consider the monochromatic data recorded for one shot, the objective function can be expressed as

$$E = \frac{1}{2} (\mathbf{u} - \mathbf{d})^T (\mathbf{u} - \mathbf{d})^* \quad (30)$$

where \mathbf{u} and \mathbf{d} are the model responses and observed data, respectively, and the superscripts T and * indicate the transpose and the complex conjugate, respectively. The gradient direction can be obtained by taking partial derivatives of eq. (30) with respect to the parameters. The gradient with respect to the k th parameter can be written by

$$\frac{\partial E}{\partial m_k} = \text{Re} \left\{ \left(\frac{\partial \mathbf{u}}{\partial m_k} \right)^T (\mathbf{u} - \mathbf{d})^* \right\} \quad (31)$$

The partial derivative waveform can be computed from the matrix equation (eq. 17) for forward modeling. Taking equation (17) with respect to the k th model parameter yields

$$\mathbf{S} \frac{\partial \mathbf{u}}{\partial m_k} = - \frac{\partial \mathbf{S}}{\partial m_k} \mathbf{u} = \mathbf{f}_v^{(k)} \quad (32)$$

$$\frac{\partial \mathbf{u}}{\partial m_k} = \mathbf{S}^{-1} \mathbf{f}_v^{(k)} \quad (33)$$

where $\mathbf{f}_v^{(k)}$ is virtual source of k th parameter. Substituting eq. (33) into eq.

(31) gives

$$\frac{\partial E}{\partial m_k} = \text{Re} \left\{ \left[\mathbf{f}_v^{(k)} \right]^T \left(\mathbf{S}^{-1} \right)^T (\mathbf{u} - \mathbf{d})^* \right\} \quad (34)$$

For the entire model parameter the gradient can be rewritten by

$$\frac{\partial E}{\partial \mathbf{m}} = \text{Re} \left\{ \left(\mathbf{F}_v \right)^T \left(\mathbf{S}^{-1} \right)^T (\mathbf{u} - \mathbf{d})^* \right\} \quad (35)$$

where \mathbf{m} is the model parameter vector, and \mathbf{F}_v is the virtual source matrix.

3.2. Verification of virtual source

In the inversion process, the gradient directions are computed by the cross-correlation of partial derivative wavefield and residuals. Because it needs many computational efforts to directly calculate the partial derivative wavefield, Pratt et al. (1998) introduced the concept of virtual source. To examine whether the virtual source is applied properly to obtain the partial derivative wavefield or not, we compare the partial derivative fields computed by different ways:

$$\frac{\partial \mathbf{u}}{\partial m_k} = \mathbf{S}^{-1} \mathbf{f}_v^{(k)} \quad , \quad (36)$$

$$\frac{\partial \mathbf{u}}{\partial m_k} = \frac{\mathbf{u}(m_k + \Delta m) - \mathbf{u}(m_k)}{\Delta m} \quad , \quad (37)$$

which will be referred to as analytic and numerical methods, respectively.

The partial derivative wavefields for acoustic wave are generated in the homogeneous and isotropic media whose size is 2 km by 2 km and velocity is 1.5 km/s. For elastic case, we use the model applied for Lamb's problem (Fig. 3). Fig.11 shows where the perturbed grid and the source are. To verify of

the virtual source, acoustic wave velocity (c) and Lamé constant (λ, μ) is perturbed in acoustic and elastic cases, respectively. The comparison of analytic and numerical methods is conducted twice, since the left- and right-side of the model use different logarithmic functions (Eq. 5). Figures 12 ~ 17 depict seismograms of the partial derivative wavefields by analytic and numerical methods. For the quantitative comparison, we extract the traces from the receiver located in the middle of the model surface (fig. 18~20). These results demonstrate that virtual source is calculated correctly and can be applied to inversion algorithm.

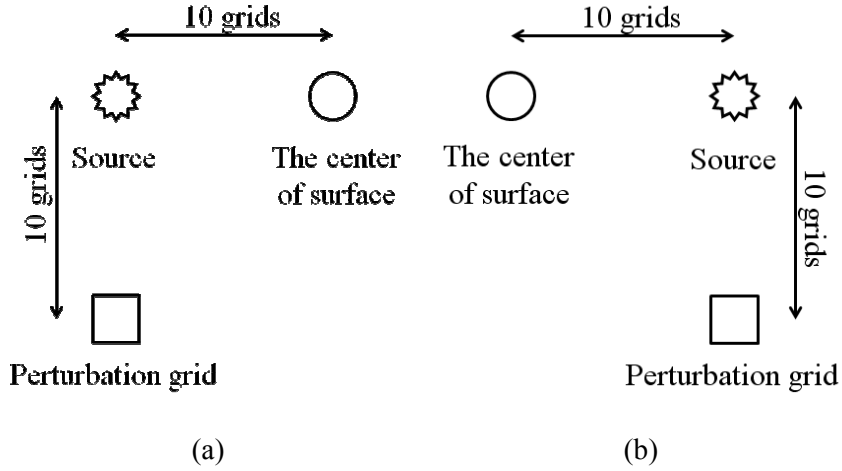


Figure 11. arrangement of the source and perturbation grid for verification of virtual source in the (a) left- and (b) right-side of the homogeneous and isotropic model

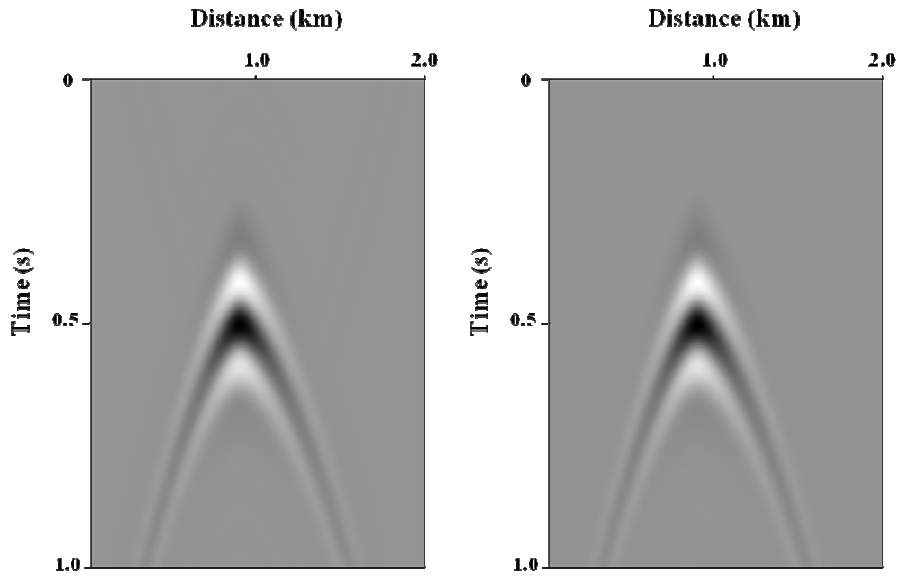


Figure 12. seismograms of partial derivative wavefields for c obtained by numerical and analytic methods for the left-side of the model

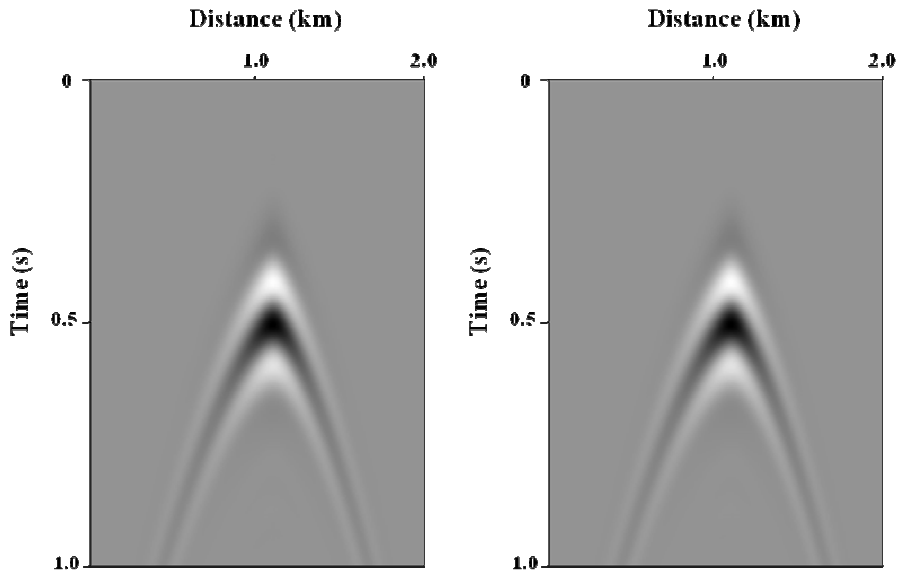


Figure 13. seismograms of partial derivative wavefields for c obtained by numerical and analytic methods for the right-side of the model

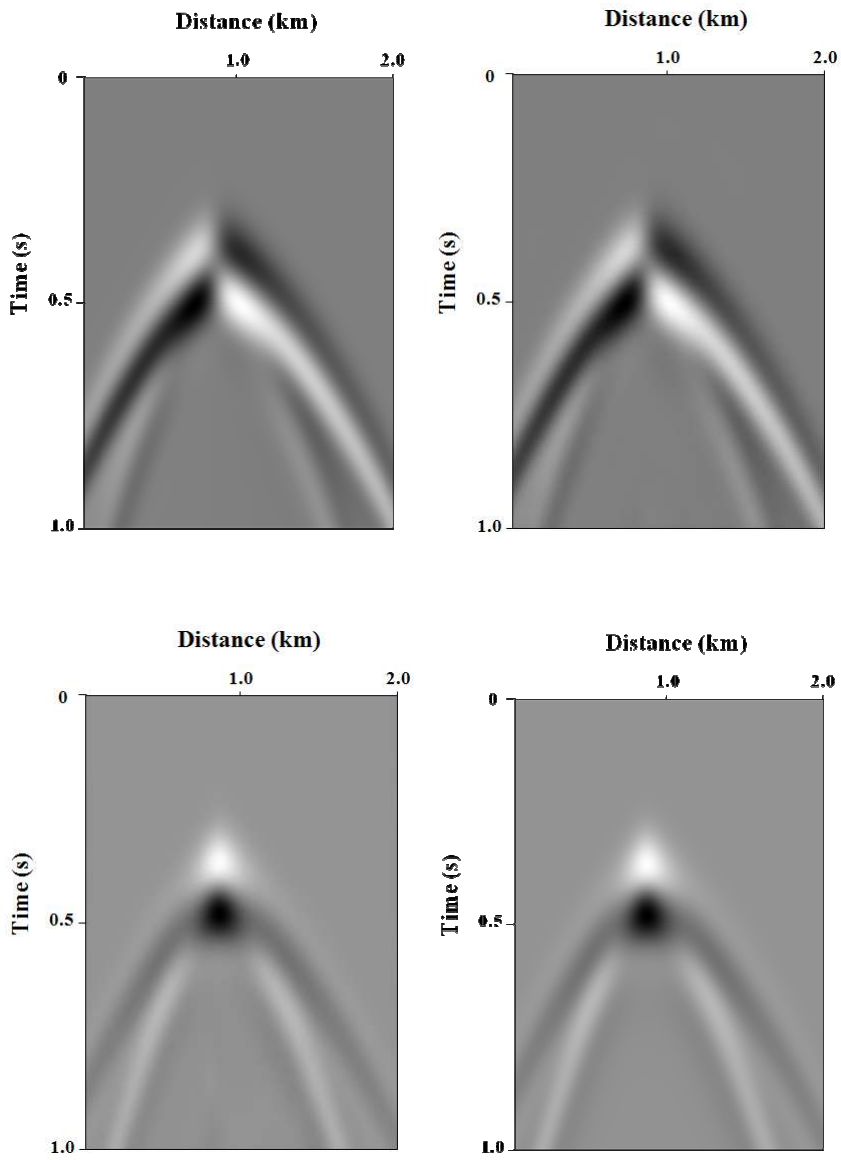


Figure 14. seismograms of partial derivative wavefields for λ obtained by numerical and analytic methods for the right-side of the model: horizontal(upper) and vertical(lower) displacements

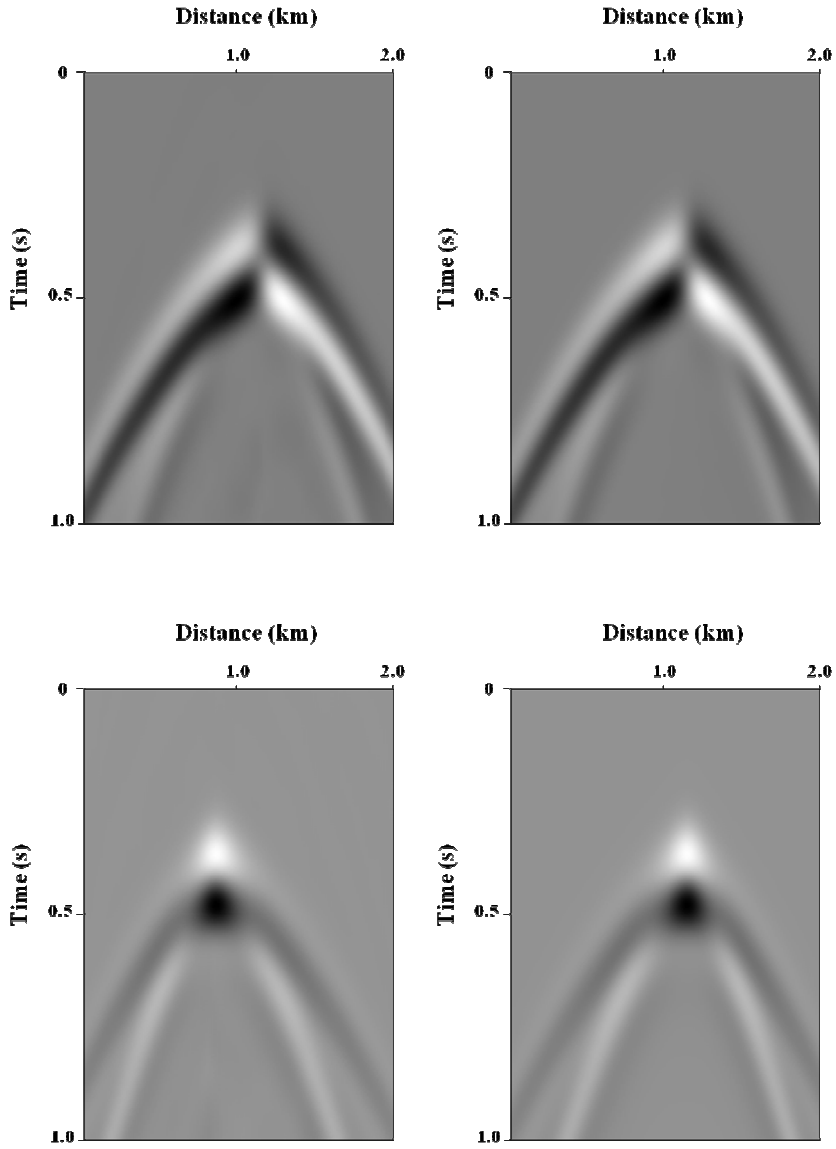


Figure 15. seismograms of partial derivative wavefields for λ obtained by numerical and analytic methods for the left-side of the model: horizontal(upper) and vertical(lower) displacements

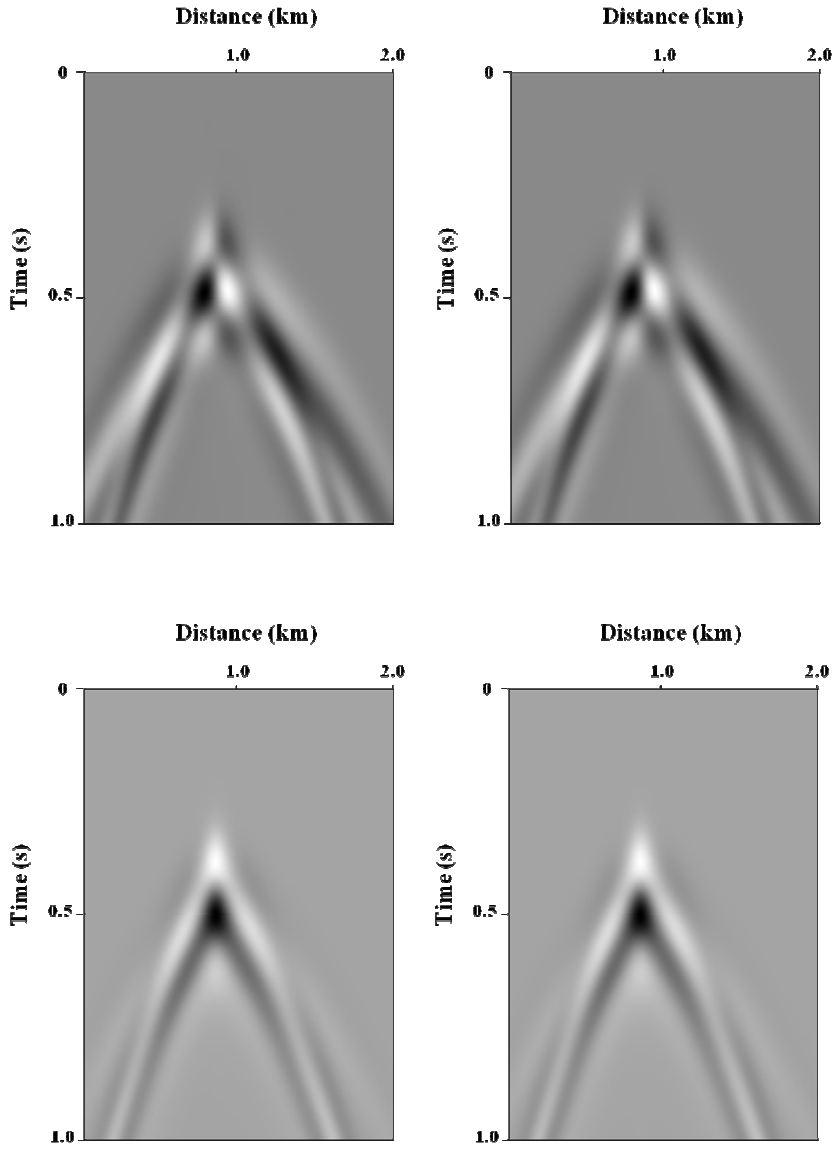


Figure 16. seismograms of partial derivative wavefields for μ obtained by numerical and analytic methods for the left-side of the model: horizontal(upper) and vertical(lower) displacements

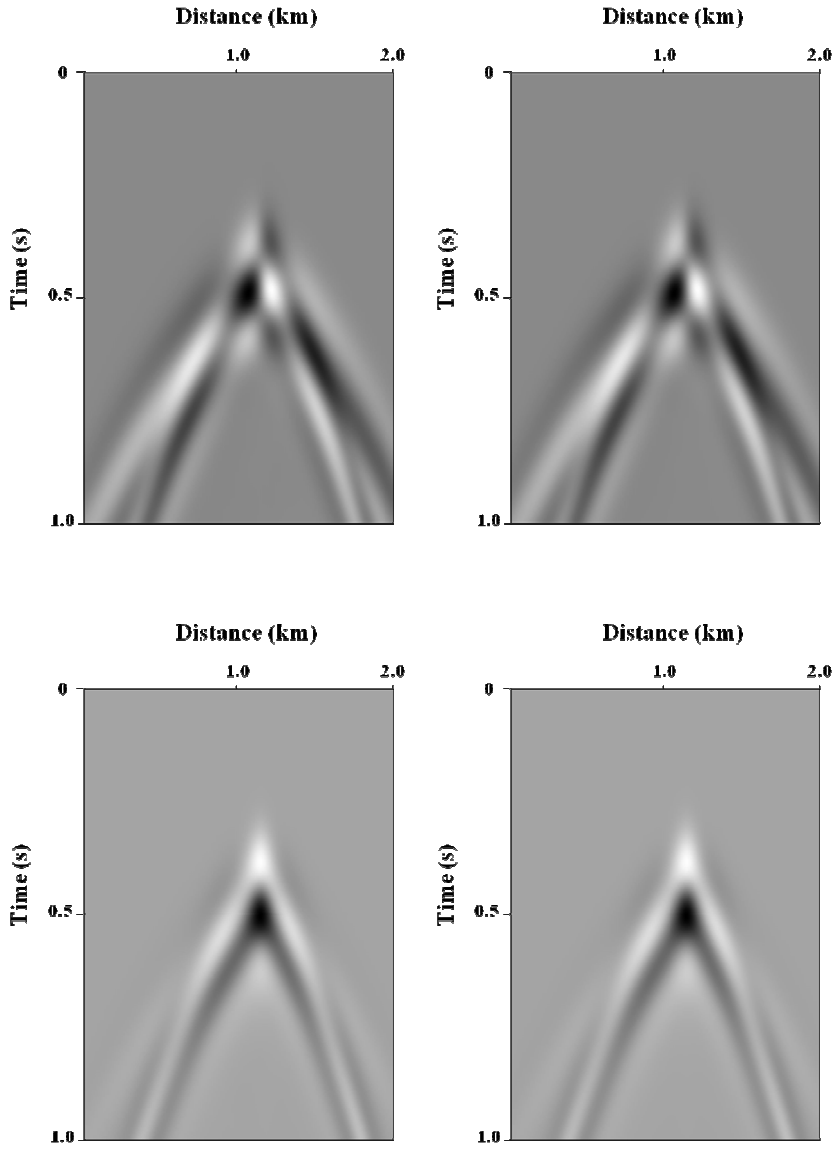


Figure 17. seismograms of partial derivative wavefields for μ obtained by numerical and analytic methods for the right-side of the model: horizontal(upper) and vertical(lower) displacements

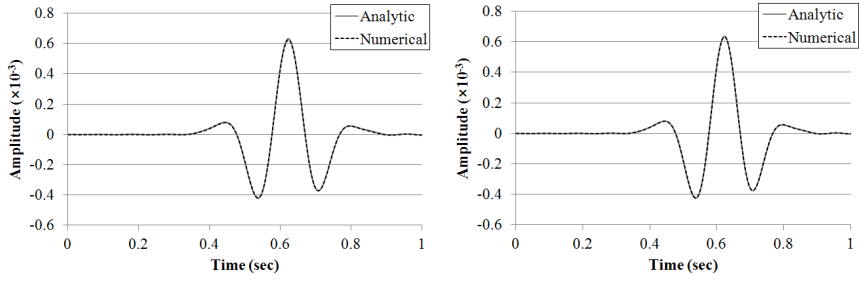


Figure 18. partial derivative wavefields of c recorded at the middle of the model for the left- and right-side of the model

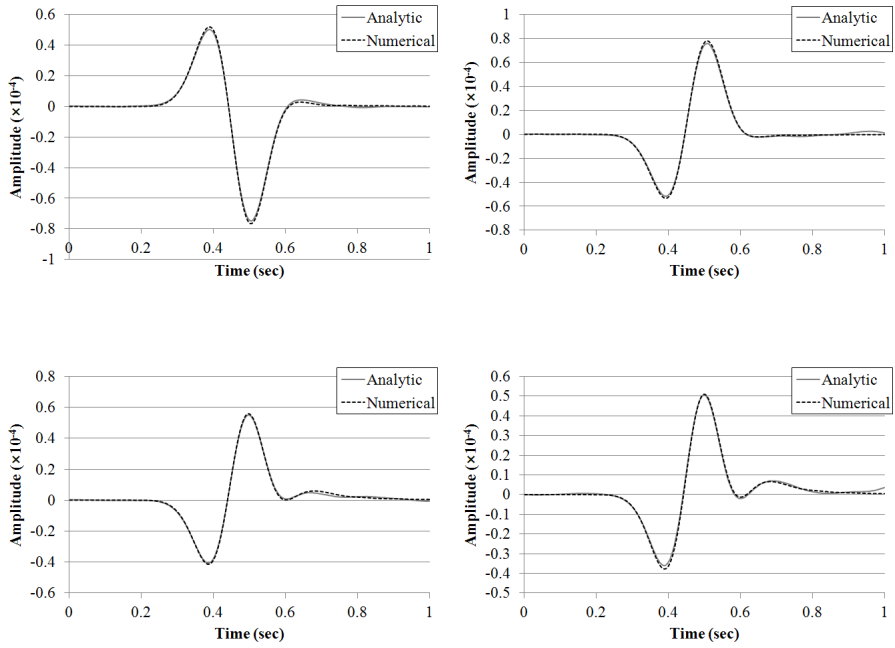


Figure 19. partial derivative wavefields of λ recorded at the middle of the model for the left- and right-side of the model: horizontal(upper) and vertical(lower) displacements

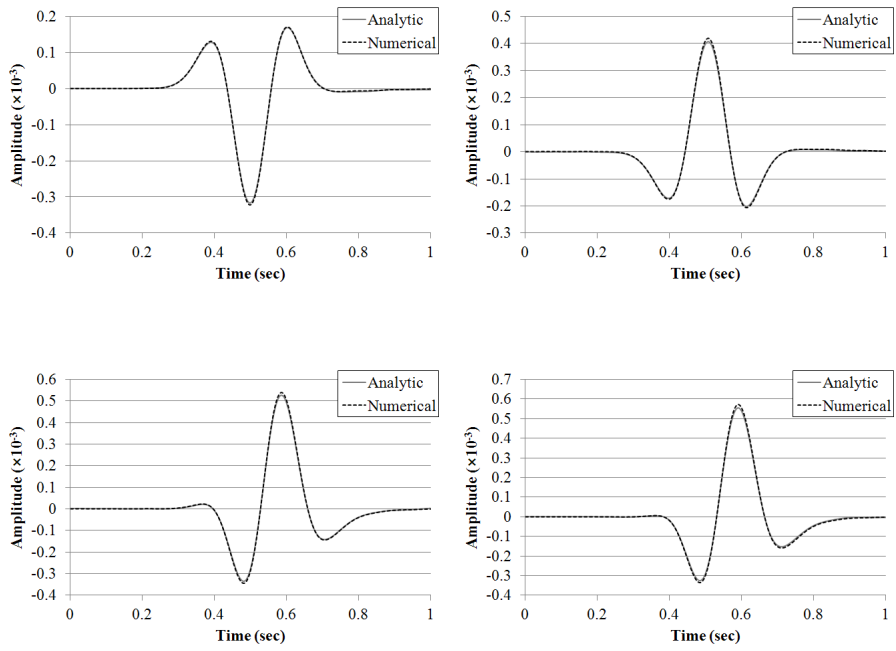


Figure 20. partial derivative wavefields of μ recorded at the middle of the model for the left- and right-side of the model: horizontal(upper) and vertical(lower) displacements

3.3. Scaling and optimization

Newton method is more accurate than gradient method because it retains terms of the misfit function expanded by a Taylor series up to quadratic order. In full Newton or Gauss-Newton method, the gradient direction is preconditioned or filtered by the inverse of full or approximate Hessian matrix. Full Hessian (\mathbf{H}) and approximate Hessian (\mathbf{H}_a) can be expressed by,

$$\mathbf{H} = \text{Re}\{\mathbf{J}'\mathbf{J}^*\} + \text{Re}\left\{\left[\left(\frac{\partial}{\partial m_1}\mathbf{J}'\right)(\mathbf{u}-\mathbf{d})^* \quad \left(\frac{\partial}{\partial m_2}\mathbf{J}'\right)(\mathbf{u}-\mathbf{d})^* \quad \cdots \quad \left(\frac{\partial}{\partial m_{np}}\mathbf{J}'\right)(\mathbf{u}-\mathbf{d})^*\right]\right\}, \quad (38)$$

$$\mathbf{H}_a = \text{Re}\{\mathbf{J}'\mathbf{J}^*\}, \quad (39)$$

where \mathbf{J} is the jacobian matrix. The second term of the full Hessian is often difficult to compute. Moreover, the first term of the full Hessian, approximate Hessian huge computing time and memory in order to calculate jacobian matrix. Shin et al. (2001) introduce pseudo Hessian matrix that estimate diagonal of the approximate Hessian matrix using virtual sources instead of jacobian matrix. In this thesis, the pseudo Hessian matrix is applied for preconditioning of the gradient direction. Since the pseudo Hessian matrix is either ill-conditioned or actually singular, a damping term is employed to regularize it and stabilize for non-linear problem (Levenberg, 1944; Marquardt, 1963). The regularized gradient at each frequency can be represented by

$$\nabla E_f = \left[\sum_s \text{diag}\{(\mathbf{F}_v)^T (\mathbf{F}_v)^*\} + \beta \mathbf{I} \right]^{-1} \left\{ \sum_s (\mathbf{F}_v)^T (\mathbf{S}^{-1})^T (\mathbf{u}-\mathbf{d})^* \right\}, \quad (40)$$

where \sum_s indicates the summation of all the shots, β is the damping term and

\mathbf{I} is the identity matrix. The gradient vector at each frequency is normalized with its largest absolute value and summed over all frequencies and this resultant gradient is normalized once again (Ha et al., 2009), as follows

$$\nabla E = \text{NRM} \sum_f \left\{ \text{NRM}(\nabla E_f) \right\}, \quad (41)$$

where \sum_f indicates the summation of all the frequency and NRM indicates the normalization operator.

We also apply the modified version (Ha et al., 2009) of the conjugate gradient method (Fletcher and Reeves, 1964). The conjugate gradient direction \mathbf{g} is obtained by

$$\mathbf{g}^{(1)} = -\nabla E^{(1)} \quad (42)$$

$$\mathbf{g}^{(n)} = -\nabla E^{(n)} + \frac{\left[\nabla E^{(n)} \right]^T \nabla E^{(n)}}{\left[\nabla E^{(n-1)} \right]^T \nabla E^{(n-1)}} \text{NRM} \left[\mathbf{g}^{(n-1)} \right] \quad (43)$$

where the superscript (n) is the iteration number and NRM is normalizing operator. The normalized conjugate gradient direction obtained in the previous iteration is used to compute the conjugate gradient direction at the present iteration. Consequently, the model parameter vector is updated by

$$\mathbf{m}^{(n+1)} = \mathbf{m}^{(n)} + \alpha \mathbf{g}^{(n)} \quad (44)$$

where α is the step length.

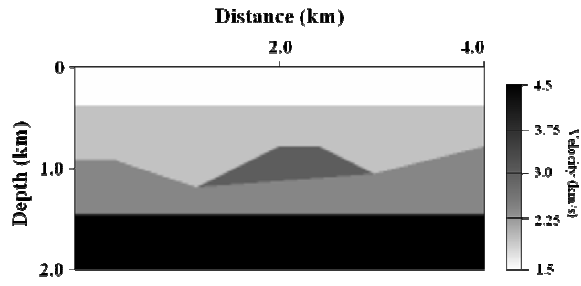
3.4. Example of inversion in the logarithmic grid set

We perform acoustic waveform inversion in the logarithmic grid set. We

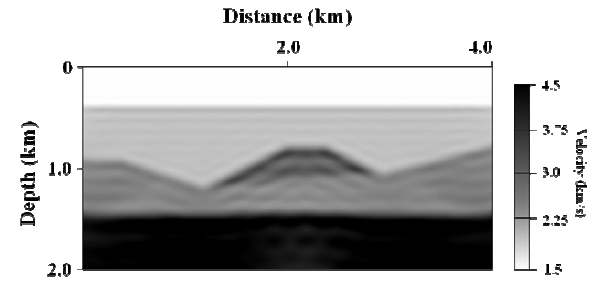
first use the simple model shown in Figure 21a, where the high-velocity layer exists in the middle of the model. The dimension of the model is 4 km by 2 km. We apply the inversion algorithms in the conventional and logarithmic grid sets to the same synthetic data generated in the conventional grid set with PML boundary condition. The maximum recording time is 3 s. We assume that 399 shot gathers are acquired with the interval of 10 m for field data. For the inversion in the logarithmic grid set, the field data should be transformed to the logarithmic grid set through interpolation. For initial guesses, the linearly increasing velocity model is used for the conventional method, whereas the exponentially increasing velocity model is employed for the logarithmic inversion.

Figures 21b and 21c show the models inverted at the 200th iteration in the conventional and logarithmic grid sets. For comparison, the model inverted in the logarithmic grid set is converted to the conventional grid set through interpolation (Figure 21d). In Figure 21, we observe that for the shallow parts the logarithmic inversion yields better results than the conventional inversion, and vice versa. Although we use the same modeling algorithm to generate both field and modeled data in the conventional inversion, the logarithmic inversion recovers the second and third layers better than the conventional method. That is, some oscillating high-frequency phenomena are observed in the second layer obtained in the conventional grid set, but it is not in the logarithmic grid set. However, the resolution of the logarithmic inversion is not as good as that of the conventional inversion for deeper part, which may be because of the logarithmically increasing grid interval in the logarithmic

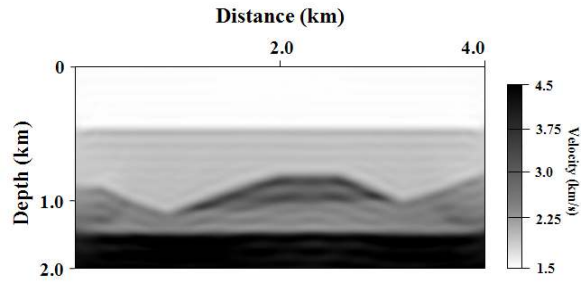
grid set. In Figure 22, we display depth profiles extracted in the middle of the inverted velocity models of Figures 21b and 21d as well as the true velocity model. Figure 22 shows that both the conventional and logarithmic inversion algorithms give reliable solutions.



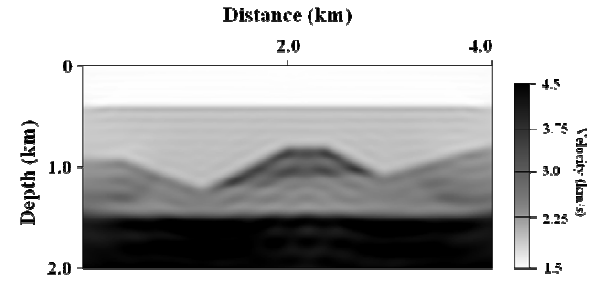
(a)



(b)



(c)



(d)

Figure 21. (a) True simple layered velocity model and inversion results obtained at the 200th iteration by using the (b) conventional and (c) logarithmic grid sets. For comparison, the logarithmic inversion result (c) is converted to the conventional grid set in (d).

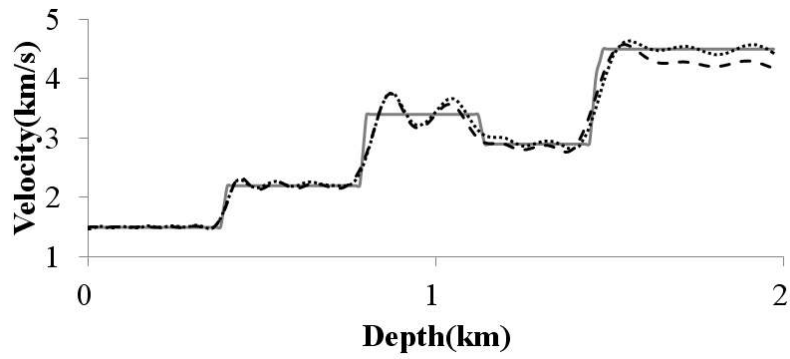
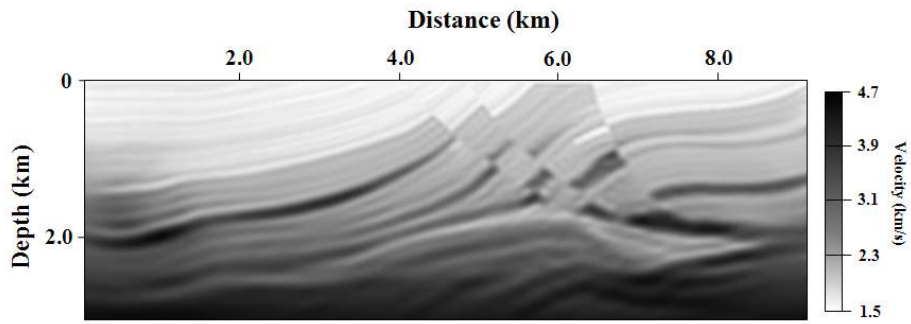


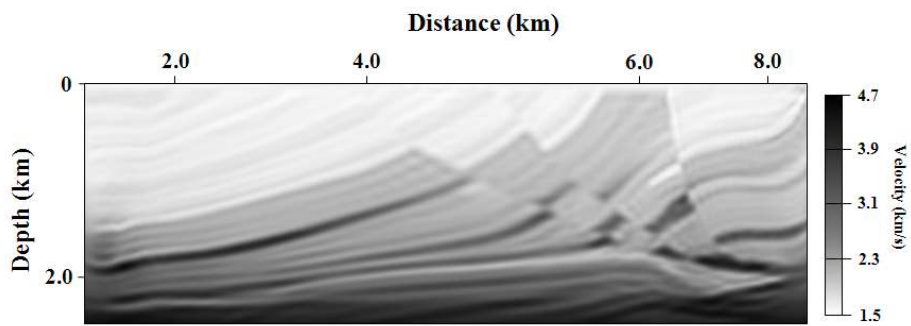
Figure 22. Depth profiles at the center of the true velocity model (solid line) and the inverted velocity models generated in the conventional (dotted line) and logarithmic (dashed line) grid sets.

We proceed to perform the inversion for the synthetic data generated in the conventional grid set for the modified version of the Marmousi-2 model (Figure 5a) for both acoustic and elastic cases. We apply both the conventional and logarithmic inversion algorithms to the same synthetic data generated in the conventional grid set with PML boundary condition.

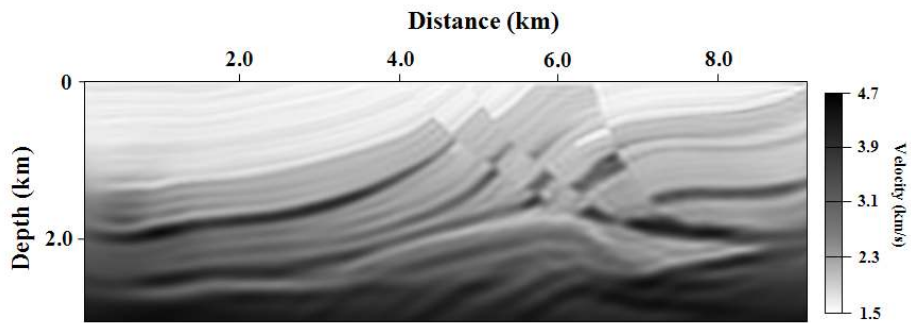
For acoustic waveform inversion, the maximum recording time is 4 s. We assume that 899 shot gathers are acquired with the interval of 10 m for field data. For the inversion in the logarithmic grid set, the field data should be transformed to the logarithmic grid set through interpolation. Figures 23a and 23b show models inverted at the 200th iteration using the conventional and logarithmic grid sets, respectively. For comparison, we also convert the model inverted in the logarithmic grid set to the conventional grid set through interpolation. Figure 24 shows depth profiles extracted from the inverted velocity models of Figures 23a and 23c as well as the true velocity model. In Figure 24, it is observed that velocities inverted by using the conventional and logarithmic grid sets are compatible with the true velocities.



(a)

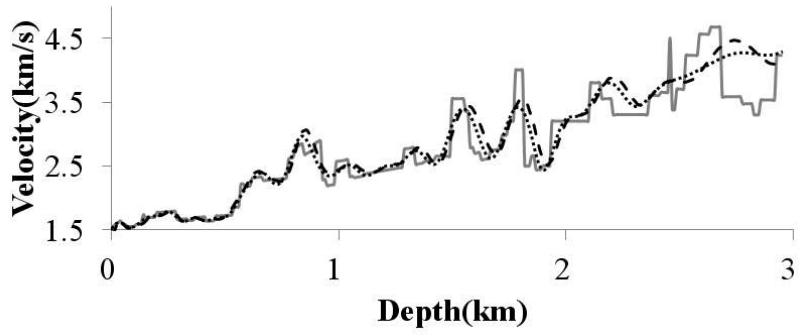


(b)

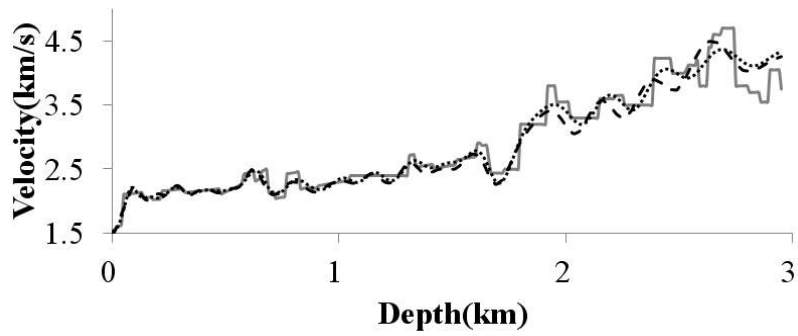


(c)

Figure 23. Inversion results obtained at the 200th iteration by using the (a) conventional and (b) logarithmic grid sets. For comparison, the logarithmic inversion result (b) is converted to the conventional grid set in (c).



(a)



(b)

Figure 24. Depth profiles at distances of (a) 4.5 km and (b) 6 km of the true velocity model (solid line) and the inverted velocity models generated in the conventional (dotted line) and logarithmic (dashed line) grid sets.

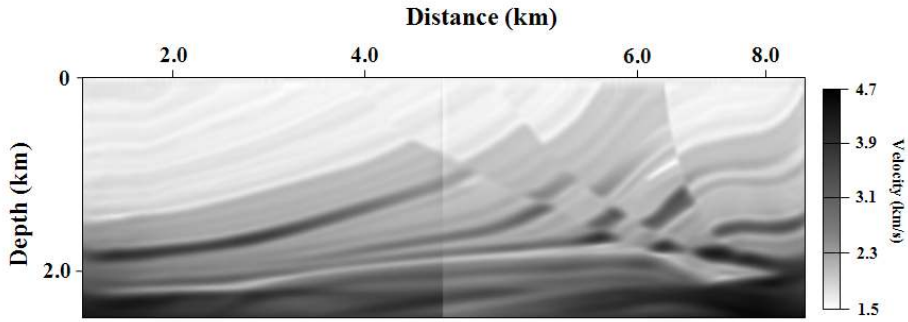
We compare the computing time required to perform acoustic waveform inversion in the conventional and logarithmic grid sets. Table 1 shows CPU times to iterate inversion process 200 times for the simple layered model and the Marmousi-2 model using 20 Intel Xeon E5640 2.66 GHz CPUs on the Linux-cluster machine. This indicates that it is more efficient to use the logarithmic grid, because we can reduce the number of grids.

However, when the recording time increases, the boundary area of the model should also increase. For too long recording time, the logarithmic inversion becomes less efficient than the conventional inversion. We may conclude that the efficiency of the waveform inversion in the logarithmic grid set is dependent on the recording time.

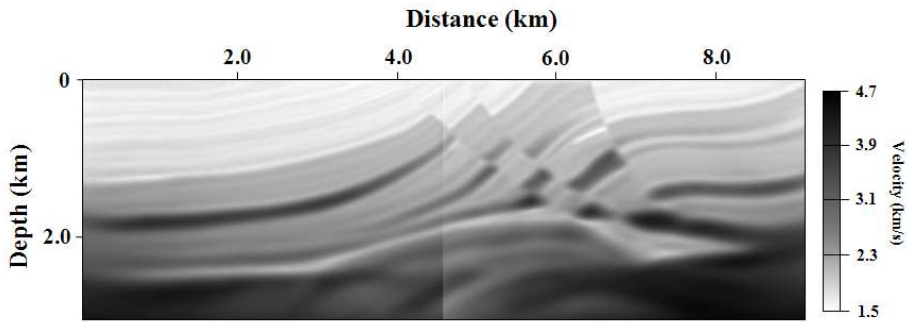
For the elastic waveform inversion, the maximum recording time is 5 s and we use 898 shot gathers for field data. In the elastic case, the frequency marching method is also employed over 5 stages: 0.2 ~ 2 Hz, 0.2 ~ 4 Hz, 0.2 ~ 6 Hz, 0.2 ~ 8 Hz, 0.2 ~ 10 Hz. For each frequency group, the inversion process is repeated for 30 iterations. Figure 25a shows the inverted model for P-wave velocity in the logarithmic set. Through interpolation, the inverted model on the logarithm scale is converted to the conventional grid set (Figure 25b). Figure 26 shows depth profiles extracted from the true and inverted P-wave velocity models for quantitative comparison. Figures 25b and 26 indicate that inversion results obtained by the new elastic waveform inversion method are comparable to true values.

Table 1. CPU times required to perform the acoustic inversion for the simple layered model and the Marmousi-2 model for 200th iteration

Model	Conventional grid set	Logarithmic grid set	Ratio (C/L)
Simple layered model	18330.65815	6323.366236	2.9
Marmousi-2 model	112242.7616	22074.23556	5.1

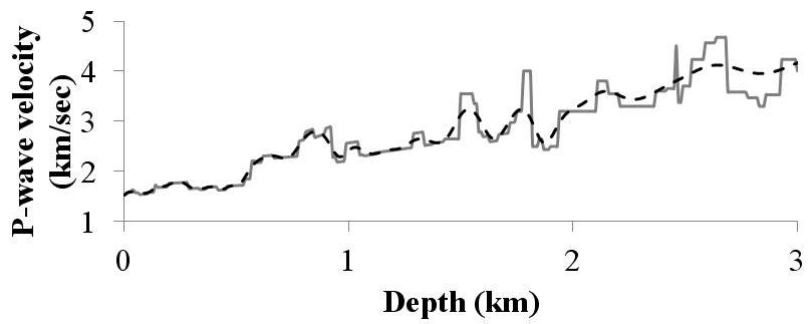


(a)

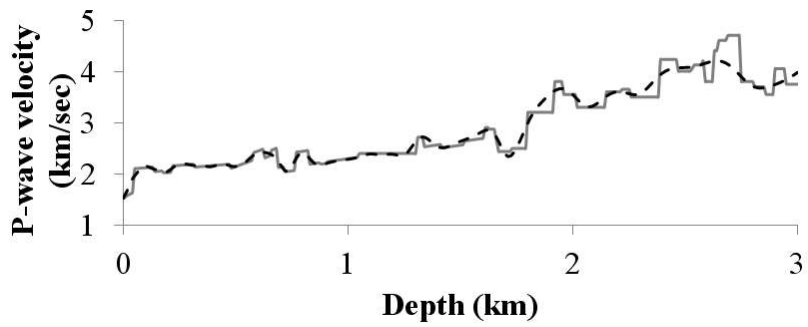


(b)

Figure 25. (a) P-wave velocity models inverted at the 200th iteration in the logarithmic grid set for the modified version of the Marmousi-2 model and (b) its interpolated version to the conventional grid set.



(a)



(b)

Figure 26. Depth profiles at distances of (a) 4.5 km and (b) 6 km of the true velocity model (solid line) and the inverted velocity models.

4. Conclusions

We developed new acoustic and elastic wave modeling and waveform inversion algorithms, which are performed in the logarithmic grid set. In the logarithmic grid set, since the grid interval increases logarithmically with distance, we require fewer grid points than in the conventional uniform grid set. Based on this feature, we can extend the given model without increasing computational efforts compared to the conventional method, so that edge reflections cannot be recorded at receivers within the recording duration. Since the number of additional grids used to extend the given model can be determined considering the recording duration, the efficiency of the new modeling and inversion algorithms is mainly dependent on the recording duration.

In order to apply the new modeling and inversion algorithms in the logarithmic grid set, interpolation is needed. Field data acquired in the conventional uniform grid should be converted to the logarithmic grid set, and inversion results on the logarithmic scale need to be converted to the conventional uniform grid set. The new modeling algorithm yielded numerical solutions compatible with analytic solutions. However, we need to know that when the source is applied near the boundary of the given model where the grid interval is large, the seismograms can suffer from numerical dispersion. We examined if the numerical dispersion is serious in waveform inversion or not. Inversion results for the simple layered model showed that the logarithmic waveform inversion yields better results for the shallow part than the conventional waveform inversion, whereas for the deeper part the

resolution of the logarithmic waveform inversion is not as good as the conventional waveform inversion. By comparing the inversion results obtained by the logarithmic waveform inversion with those of the conventional method for the modified version of the Marmousi-2 model, we showed that the new logarithmic waveform inversion can be applied to the complicated model with computation efficiency. From all the inversion results, we noted that numerical dispersion does not seriously influence inversion results. The frequency marching method may contribute to reducing the influences of numerical dispersion in high frequencies. Although we only test the new modeling and inversion algorithms to 2D problems, their efficiency will be greater in 3D problems. We also feel that the new modeling and inversion methods may contribute to improving the efficiency of data acquisition.

References

- Bunks, C., F. M. Saleck, S. Zaleski, and G. Chavent, 1995, Multiscale seismic waveform inversion: *Geophysics*, **60**, 1457–1473.
- Cerjan, C., D. Kosloff, R. Kosloff, and M. Reshef, 1985, A nonreflecting boundary condition for discrete acoustic and elastic wave equation: *Geophysics*, **50**, 705-708.
- Clayton, R., and B. Enquist, 1977, Absorbing boundary conditions for acoustic and elastic wave equations: *Bulletin of the Seismological of America*, **67**, 1529-1540.
- Collino, F., and C. Tsogka, 2001, Application of the PML absorbing layer model to the linear elastodynamic problem in anisotropic heterogeneous media: *Geophysics*, **66**, 294–307.
- Ewing, W. M., W. S. Jardetzky, and F. Press, 1957, *Elastic waves in layered media*: McGraw-Hill.
- Fletcher, R., and C. M. Reeves, 1964, Function minimization by conjugate gradient: *The Computer Journal*, **7**, 149-154.
- Ha, W., and C. Shin, 2012, Efficient Laplace-domain modeling and inversion using an axis transformation technique: *Geophysics*, **77**, R141-R148.
- Ha, T., W. Chung, and C. Shin, 2009, Waveform inversion using a back-propagation algorithm and a Huber function: *Geophysics*, **74**, no.3, R15–R24.
- Higdon, R. L., 1991, Absorbing boundary conditions for elastic waves, *Geophysics*, **56**, 231-241.
- Jastram, C., and E. Tessmer, 1994, Elastic modeling on a grid with vertically

- varying spacing, *Geophysical Prospecting*, **42**, 357–370.
- Kim, Y., H. Cho, D.-J. Min, and C. Shin, 2011, Comparison of frequency-selection strategies for 2D frequency-domain acoustic waveform inversion: *Pure and Applied Geophysics*, **168**, 1715–1727.
- Lailly, P., 1983, The seismic inverse problem as a sequence of before stack migration, in J. B. Bednar, R. Rednar, E. Robinson, and A. Weglein, eds., *Conference on inverse scattering: Theory and application: Society for Industrial and Applied Mathematics*, 206–220.
- Martin, G. S., R. Wiley, and K. J. Marfurt, 2006, Marmousi2: An elastic upgrade for Marmousi: *The Leading Edge*, **25**, 156–166.
- Min, D.-J., C. Shin, and H. S. Yoo, 2004, Free-surface boundary condition in finite-difference elastic wave modeling: *Bulletin of the Seismological of America*, **94**, 237–250.
- Moczo, P., 1989, Finite-difference technique for SH waves in 2-D media using irregular grids: application to the seismic response problem, *Geophysical Journal International*, **99**, 321–329.
- Pratt, R.G., and M.H. Worthington, 1990, Inversion theory applied to multi-source crosshole tomography. Part 1: Acoustic wave equation: *Geophysical Prospecting*, **38**, 287-310.
- Pratt, R.G., C. Shin, and G.J. Hicks, 1998, Gauss-Newton and full Newton methods in frequency-space seismic waveform inversion: *Geophysical Journal International*, **133**, 341-362.
- Reynolds, A.C., 1978, Boundary conditions for the numerical solution of wave propagation problems: *Geophysics*, **43**, 1099-1110.

- Roach, G. F., 1982, Green's functions (2nd ed.): Cambridge University Press.
- Shin, C., 1995, Sponge boundary condition for frequency-domain modeling: *Geophysics*, **60**, 1870-1874.
- Shin, C., S. Jang, and D.-J. Min, 2001, Improved amplitude preservation for prestack depth migration by inverse scattering theory: *Geophysical Prospecting*, **49**, 592–606.
- Tarantola, A., 1984, Inversion of seismic reflection data in the acoustic approximation: *Geophysics*, **49**, 1259-1266.

초 록

로그 격자군을 이용한 주파수 영역에서의 음향파 및 탄성과 모델링과 파형 역산

최 승 우

에너지시스템공학부

서울대학교 대학원

경계조건은 탄성과 모델링의 정확성에 영향을 주는 요인 중 하나이다. 지금까지 개발된 여러 종류의 경계조건들은 각자의 장점과 단점을 가지고 있다. 모델의 크기를 확장시킴으로써 모델의 경계에서 발생하는 반사파가 수진기에 기록되지 않게 하는 방법을 통해 이러한 반사파를 완벽하게 없앨 수 있다. 모델의 크기를 키우면서 계산 비용을 증가시키지 않게 하기 위해서, 로그 격자군에서의 음향파 및 탄성과의 모델링 알고리즘을 제안하고자 한다. 로그 격자군이란 모델 표면의 중앙으로부터 격자의 크기가 대수적으로 증가하는 격자군을 의미한다. 이 방법은 로그 스케일의 성질에 의해 격자의 개수를 줄일 수 있는 장점이 있다. 음향파 및 탄성과 모델링을 로그 격자군에서 수행하기 위하여, 우선 균등한 스케일에서의 파동 방정식을 로그 스케일로 변환시켜야 한다. 그 다음, 음향파 모델링의 경우에는 일반적인 유한 차분법을, 탄성과 모델링의 경우에는 셀 기반의 유한 차분법을 적용시킨다. 수치 예제들은 새로운 모델링 알고리즘이 송신원이 큰 격자에 위치한 경우 분산에 의한 영향을 보여주지만, 일반적으로 사용되는 모델링의 결과와 비슷한 결과를 제시하는 것을 보여준다. 단순한 층 구조와 마무시-2 모델에서의 역산 결과들은 로그 격자군에서의 역산 알고리즘 역시 일반 격자와 비슷한 결

과를 내는 것을 보여준다. 뿐만 아니라, 분산에 의한 효과는 거의 무시할 만 하며, 기록 시간이 길지 않을 경우 계산량이 줄어드는 효과가 있다.

주요어 : 음향파, 탄성파, 모델링, 파형 역산, 로그 격자군
학 번 : 2011-21113